# NUMERICAL HOMOGENIZATION OF A ROUGH BI-MATERIAL INTERFACE

A Thesis
Presented to
The Academic Faculty

by

Lucas Lallemant

In Partial Fulfillment
of the Requirements for the Degree
Master of Science in the
School of Mechanical Engineering

Georgia Institute of Technology
August 2010

# NUMERICAL HOMOGENIZATION OF A ROUGH BI-MATERIAL INTERFACE

Approved by:

Dr. Mohammed Cherkaoui, Advisor
School of Mechanical Engineering
*Georgia Institute of Technology*

Dr. Laurent Capolungo
School of Mechanical Engineering
*Georgia Institute of Technology*

Dr. Olaf van der Sluis
Department of Mechanical Engineering
*Philips & Eindhoven University of Technology, Eindhoven, The Netherlands*

Dr. Tudor Balan
Department of Mechanical Engineering
*Georgia Institute of Technology & Arts et Metiers ParisTech, Metz, France*

Date Approved: 6 May 2011

# TABLE OF CONTENTS

# LIST OF TABLES

# LIST OF FIGURES

# NOMENCLATURE

## List of symbols

| | |
|---|---|
| $a$ | crack length |
| $a_0$ | initial crack length |
| $\beta$ | shear to normal ratio |
| $C$ | compliance |
| $\delta$ | threshold for friction |
| $\delta_{ij}$ | Kronecker symbol |
| $\vec{\delta}$ | interface opening vector |
| $\epsilon$ | strain tensor |
| $\epsilon_e$ | elastic strain tensor |
| $\epsilon_p$ | plastic strain tensor |
| $E$ | Young modulus |
| $F$ | force |
| $\Gamma_u^m$ | microscopic displacement boundary |
| $\Gamma_t^m$ | microscopic traction boundary |
| $\Gamma_{int}^m$ | microscopic interface |
| $\Gamma_u^M$ | macroscopic displacement boundary |
| $\Gamma_t^M$ | macroscopic traction boundary |
| $G$ | Energy release rate |
| $G_c$ | interface toughness |
| $G_R$ | crack kinking criterion |
| $2h$ | height of the specimen for a benchmark |
| $h1$, $h2$ | heights of the upper and lower layers of the RVE |
| $I$ | second moment of area |
| $K$ | virgin stiffness |

| | |
|---|---|
| $k1$ and $k2$ | delamination selection parameters for 3ENF |
| $L$ | length of the specimen for a benchmark |
| $2\lambda$ | period of the roughness profile |
| $\lambda$ | effective displacement |
| $\lambda_c$ | critical displacement |
| $\mu$ | friction coefficient |
| $N$ | number or recorded points in a simulation |
| $\vec{n}$ | normal vector |
| $\nu$ | Poisson ratio |
| $Q$ | history variable |
| $2R$ | depth of the roughness profile |
| $s$ | local curvilinear coordinate |
| $2S_0$ | length of the flat part of the roughness profile |
| $\sigma^m$ | microscopic stress tensor |
| $\sigma^M$ | macroscopic stress tensor |
| $\sigma_y$ | yield stress |
| $\vec{t}$ | traction vector |
| $\tau$ | effective traction |
| $\tau_{max}$ | tensile strength |
| $\theta$ | loading angle |
| $\theta_c$ | critical loading angle |
| $\vec{u}$ | microscopic displacement vector |
| $\vec{u^M}$ | macroscopic displacement vector |
| $\tilde{u}$ | displacement fluctuation |
| $w$ | width of the specimen for a benchmark |
| $W$ | work |
| $\Omega_m$ | domain |

| | |
|---|---|
| $I, II$ and $III$ | principal direction |
| 0 | boundary condition |
| 1 | bottom left hand corner vertex |
| $I$ | mode I (normal loading) |
| 2 | bottom right hand corner vertex |
| $II$ | mode II (shear loading) |
| 3 | top right hand corner vertex |
| 4 | top left hand corner vertex |
| $B$ | bottom side of the RVE |
| $de$ | delimination end |
| $ds$ | delimination start |
| $f$ | friction |
| $fit$ | value on the fitting function |
| $i$ or $int$ | interface |
| $L$ | left side of the RVE |
| $m$ | microscopic scale |
| $M$ | macroscopic scale |
| $n$ | normal |
| $p$ | polymer |
| $R$ | right side of the RVE |
| $sim$ | value from the simulation |
| $T$ | top side of the RVE |
| $t$ | tangential |
| $tot$ | total |

| | |
|---|---|
| 3ENF | 3-point bend End-Notched Flexure |
| ARE | Area Release Energy |
| CZE | Cohesive Zone Element |
| DCB | Double Cantilever Beam |
| EMC | Epoxy Mold Compound |
| ERR | Energy Release Rate |
| RVE | Representative Volume Element |
| TSL | Traction-Separation Law |
| VCCT | Virtual Crack Closure Technique |

# ACKNOWLEDGEMENT

I would like to thank Mohammed Cherkaoui who has given me the opportunity to work on this project. During my thesis he has been my main supervisor from Georgia Tech. I would also like to thank Olaf van der Sluis for having supervised my work during my internship at Philips Research Eindhoven and during my semester at Georgia Tech. Tudor Balan also deserves thanks. He has been my main supervisor from Arts&Métiers Paristech. I would also like to thank Laurent Capolungo for joining the reading committee for the defense of my thesis. Josyane Roschitz and Glenda Johnson were helpful as well. They provided me with adminsitrative services which was greatly appreciated.

I would also like to thank Ger Janssen, Roy Engeler, Alexandru Opran, Peter Timmermans, Sergei Shulepov, Marco Baragona, Ruud Voncker, Bruno Frackowiak, Geneviève Martin, and the rest of the Philips staff. I would also like to recognize the interns at Philips in the Netherlands. They provided me with friendship and good memories.

I would like to thank my fraternity brothers in Delta Upsilon with whom I have shared many great experiences. As a proof of brotherhood, my fraternity brothers, Justin Barstow, Devin Johnson, Matthiew Kazmier, Sasha Eslami, Tanveer Chandok, Max Kipp, Reid Harrison, Joe Miller, Phil Oliver and Matus Jiraboondilok, helped me review this report.

I would like to thank Kotaro Fukasaku and Jean-Baptiste Bouquet who worked on this project with me from start to finish.

Finally, I would like to thank my family and my parents who supported me during this project.

# CHAPTER I

## INTRODUCTION

The range of materials used in an electronic component has dramatically increased with the size reduction of electronic devices. The mechanical reliability of these components has become harder and harder to predict due to the different damage mechanisms occurring, as described in Figure 1. The delamination mechanism which consists of the separation of two different bonded materials has become crucial in the damage process. The accuracy in modeling this phenomenon is a very challenging issue that is investigated in the Nano Interface Project [17]. The aim of this project is to set up a numerical simulation tool starting at the atomic scale. One of the applications will be characterizing the bonds between the different materials involved in the Systems in Package. This will reduce the use of expensive experimental testing in the design of electronic devices.

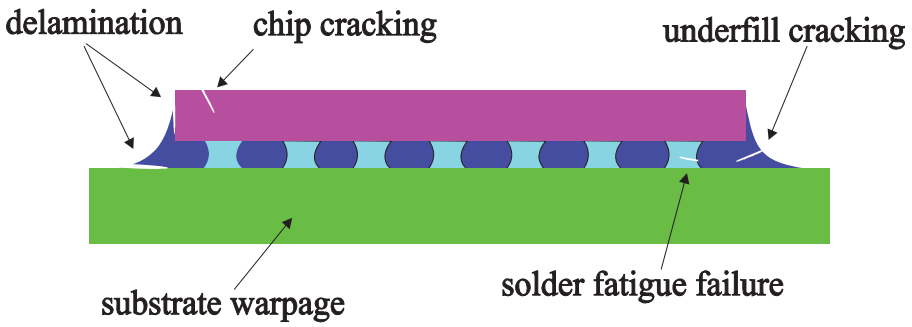


Figure 1: Different damage processes in a flip-chip package [35]

Many mechanisms are involved when two material are bound in the adhesion process. At the molecular scale. Diffusion, interdiffusion, Lifshitz-Van der Waals interaction, molecular interaction (acid-base interaction), and chemical adhesion (covalent liaisons) result in an overall adhesive force [35]. Unfortunately, the overall adhesion force does not fully define

the resulting macroscopic adhesion. A complex roughness profile characterizes the contact between the two materials which modifies the behavior of the interface. Naturally, the macroscopic adhesion force will be enhanced by the increase of contact area. These adhesions forces will also be strongly modified by several dissipative effects occurring around the rough interface. These forces include the friction at the interface as well as the plasticity and other damage processes in the bulk materials. The main area of difficulty is incorporating all these dissipative effects occurring at the microscopic scale into so-called homogenized parameters reflecting the behavior of the interface at the macroscopic scale. This task is not straightforward because there are complex numerical calculations used to accurately model these dissipative mechanisms.

Usually, the cohesive properties characterizing the bond between two materials on a flat interfaces are determined by the use of benchmarks [4, 7, 36]. These benchmarks use the beam theory enhanced with fracture mechanics which is a commonly used technique. These tests can be implemented in a Finite Element Method software. Unfortunately, the FEM simulations do not accurately depict the effects occurring at the microscale. Numerically, the models results would not be accurate because the computer would require a large number of elements and the solvers would not always give converging results. This thesis aims at providing a homogenization method to lump all microscopic dissipation mechanisms into the macroscopic cohesive properties. In this report, the behavior of the interface will be studied on a small portion, the Representative Volume Element. The difficulty is to define the right boundary conditions and loadings to ensure the RVE is behaving in a realistic manner. Afterwards, the transition from the microscopic state variables to the macroscopic state variables will be computed using the macroscopic Traction Separation Law. Since the dissipative effects are more pronounced for shear loading, the cohesive properties are dependent on mode angle. For this reason, the experiment will be performed using mixed mode loading.

Chapter II will present elements about the delamination process and an overview of fracture mechanics. Then, the representation of the adhesive forces using Cohesive Zones Elements (CZE) will be explained. At this point, some of the dissipative mechanisms

occuring at the microscale will be explained as well. In chapter III, a method used to extract the cohesive properties will be presented. In chapter IV, the method to implement these mechanisms using a FEM software will be described. Two benchmarks will also be modeled to validate the results of the homogenization method on a simplified rough interface. These results will be presented in the first section of chapter V, followed by an explanation of the contact description. Finally, the last section is a description of the results of the homogenization method applied to a copper - EMC interface.

# CHAPTER II

# THEORY ABOUT DELAMINATION

## *2.1 An overview of fracture mechanics*

Fracture mechanics is the field of mechanics dealing with crack propagation in a material. The classical approach is to study the effects of an external loading in a material with an existing crack. In some situations, it allows to predict the evolution of the crack depending on its dimensions and position with respect to the applied loading. The loading is characterized by its direction with respect to the crack, named as mode angle. Any loading can be described as the superposition of three main mode angles, which are depicted in Figure 2. Any combination of these modes is called mixed-mode loading.[5]

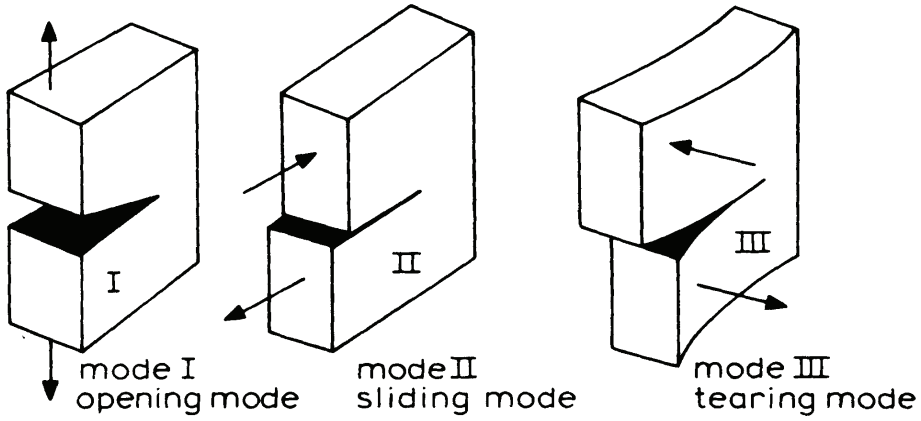


Figure 2: Loading modes [27]

An energy-based criterion is defined for linear elastic materials in Griffith's theory [8, 14] to determine whether the crack will propagate. Let us first write the balance of energy for a propagating crack in a system on which a force field is applied. A virtual area increasing $\delta A$ of the crack generates an energy $G\delta A$.

$$\delta P = -G\delta A \tag{1}$$

Here, G represents the energy release rate, the energy available for crack propagation per area unit, expressed in J/m$^2$ or N/m. The potential energy of the system $P$ can be

linked to the work of elastic deformations $W$, and the work of the applied forces $T_{ext}$ as follows:

$$P = W - T_{ext} \tag{2}$$

There is threshold value $G_c$ called fracture toughness for which the crack produces more energy than it produces. In this case, the crack propagation is not stable:

$$G\delta A > G_c \delta A \tag{3}$$

Combining equations 1 and 2 allow an analytical expression of the energy release rate for a linear material behavior. Let us consider a system containing a crack of length $a$, loaded by a constant force $F$. We assume that the evolution of the force is linear with respect to the displacement value $u$ of the application point:

$$u = CF \tag{4}$$

Here, the compliance $C$ depends on the stiffness of the material, the geometry, and also the crack length $a$. Let us consider a virtual increase of the crack length $\delta a$. This results in a variation of the elastic deformation $\delta W$ and the work of the external force $\delta T_{ext}$:

$$\delta W = \delta \left( \frac{1}{2} F u \right) \delta T_{ext} = \delta \left( F u \right) \tag{5}$$

We can then write the expression of the toughness:

$$G = \frac{F^2}{2e} \frac{dC}{da} \tag{6}$$

Another approach has been proposed by Irwin [13]. He described the stress field on a point $M$ around the crack tip of a loaded structure. Each term $\sigma ij$ of the stress tensor is proportional to $\frac{1}{\sqrt{2\pi r}}$, where r is the distance to the crack tip, multiplied by a function $f_{ij}$, taking in account the shape of the structure.

$$\sigma_{ij}(M) = \frac{K}{\sqrt{2\pi r}} f_{ij}(M) + o(r) \tag{7}$$

The parameter $K$ is the stress intensity factor. It is different for each mode angle (figure 2) . The theory of plane elasticity can be used to determine an expression of K in the general case:

$$K = \alpha \sigma \sqrt{\pi a} \tag{8}$$

The parameter $\alpha$ is a correction term taking into consideration the shape of the crack and configuration of the loading. It is possible to link the intensity factor with the energy release rate. For an elastic material with stiffness $E$ and Poisson ratio $\nu$, we have:

$$\begin{cases} G = \frac{K^2}{E}(1-\nu^2) & \text{for plane strain} \\ G = \frac{K^2}{E} & \text{for plane stress} \end{cases} \tag{9}$$

Many techniques deal with the determination of the energy released rate for finite element models. The J-Integral has been set up by Eshelby [6] for elastic materials. This integrand is performed on an arbitrary path surrounding the crack tip. The value is equal to zero if no crack is present. It has been proved that when plasticity is neglected, this integrand equals the energy release rate.

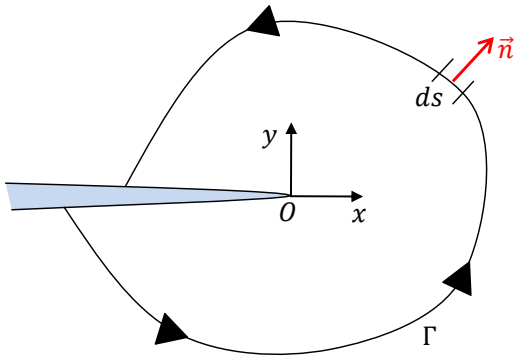


$$\begin{cases} J = \int_\Gamma w dy - t_i \frac{\partial u_i}{\partial x} ds \\ w = \int_0^\epsilon \bar{\bar{\sigma}}\, d\bar{\bar{\epsilon}} \end{cases}$$

Figure 3: The J-integral

The Virtual Crack Closure Technique (VCCT), fully explained in [18], is another method to evaluate the energy release rate. The crack is modeled in a FEM model by nodes having the same coordinates but not connected together. Under an external loading, the mesh on each part of the represented crack can then deform independently, as illustrated in figure 4. The crack propagation can be represented by successively releasing the nodes on an assumed crack path. The energy dissipated during the crack propagation can be computed by considering the variation of work at the crack tip when the next node on the path is released. With the VCCT method, only one configuration with a given crack length is actually represented. On figure 4, consider the configuration where the crack has the length $a$, i.e. when the nodes $l$ and $l^*$ were connected. The actual configuration represents a crack

propagation $\Delta a$ in which the nodes $l$ and $l*$ are now released and have respective vertical and horizontal displacements $w_l$, $u_l$, $w_{l*}$ and $u_{l*}$ due to the external loading. The shear and opening forces on the crack tip, respectively $X_i$ and $Z_i$ on node i, are assumed to have the same value when the crack had the length $a$. The assumption is that the energy necessary to "open" the crack is the same as the energy needed to close it. This allows the following expression for the energy release rate to be written as:

$$\begin{cases} GI = -Z_i \frac{(w_l - w_{l*})}{2\Delta a} & \text{for mode I} \\ GII = -Z_i \frac{(u_l - u_{l*})}{2\Delta a} & \text{for mode II} \end{cases} \tag{10}$$

The VCCT has the advantage of not having severe assumption on the material properties. However, a symmetric mesh is required in the model.

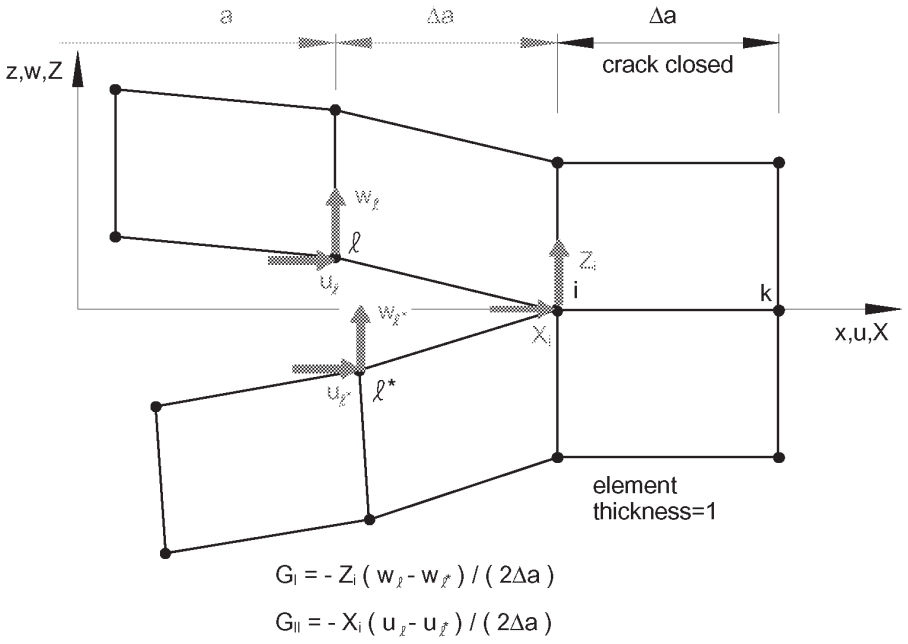


Figure 4: The VCCT [18]

These two methods are interesting, but they cannot be applied directly if an existing crack is not represented. One way to represent crack nucleation is the Area Release Energy (ARE) method. It delivers an estimation of the risk of delamination at an interface [32]. The advantage of this technique is that it can be applied for complex 3D structures. An energy release area value is calculated in a finite element model by suppressing the links

of the nodes surrounding an observed point. The advantage of performing the calculation over a small area around the observed point is to get rid of the mesh dependency.

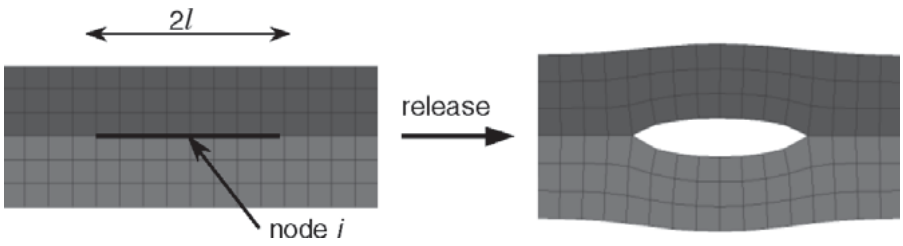


$$G_i = \frac{1}{2A_i}\vec{F_j}.\vec{u_j} \qquad A_i : released\ area$$

Figure 5: The ARE [32]

These methods based on the evaluation of the interface toughness do not appear very efficient for modeling crack propagation. For a given loading, the model has to be re-meshed several times before the equilibrium is reached, in other words, until the determination of another crack length allowing an energy release rate value smaller than the toughness at the crack tip. We chose to use Cohesive Zone Elements (CZE) to model the adhesion between the layers [33, 26]. This approach allows combining both crack nucleation and propagation without computationally expensive re-meshing. In a finite element model, specific elements are inserted between the materials which might experience delamination. The adhesive forces are represented by a traction-separation law.

### *2.2 The Cohesive Zone Elements (CZE)*

Several models have been developed to define the behavior of the CZE. They are summarized in [3]. Here, we will develop more on the exponential model which is already implemented in the finite element software used for the simulations and explained in [33]. Relations between the traction (in $N/mm^2$) and the separation vectors, respectively $\vec{t}$ and $\vec{\delta}$, are defined using scalar equivalents:

$$\lambda = \sqrt{\langle \delta_n \rangle^2 + \beta^2 \delta_s^2} \qquad ; \qquad \tau = \sqrt{t_n^2 + \beta^{-2} t_s^2} \tag{11}$$

Here, $\langle x \rangle = \dfrac{x + |x|}{2}$ are McAuley brackets. The subscripts $n$ and $s$ stand respectively for the normal and shear components. As a result of the McAuley brackets, the effective

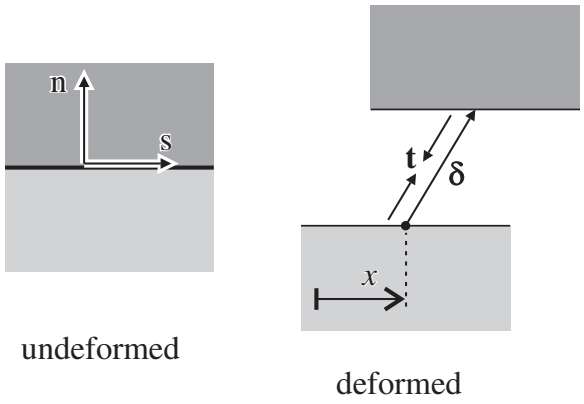


Figure 6: Traction and displacement vectors [33]

displacement does not take in account the negative part of the normal separation, which corresponds to inter-penetration between the two layers. These inter-penetration must be prevented with the help of additional contact equations. $\beta$ is the shear to normal ratio, defined by:

$$\beta = \frac{t_{s,max}}{t_{n,max}} \tag{12}$$

The relation linking the effective traction and separation is defined by the so-called traction-separation law (TSL). As it has been written above, we will use an exponential law which is more robust in comparison with linear models, due to the continuity of the function.

$$\tau = \tau_{max} \frac{\lambda}{\lambda_c} exp\left(1 - \frac{\lambda}{\lambda_c}\right) \tag{13}$$

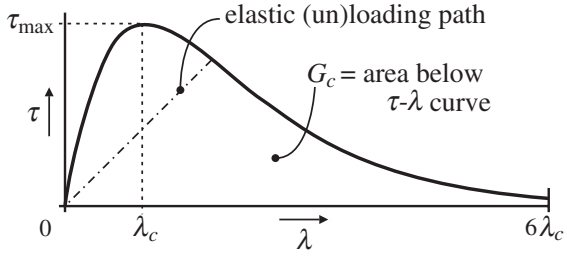


Figure 7: Effective traction-separation curve [33]

This law is fully described by two constitutive parameters, the tensile strength $\tau_{max}$ and the critical displacement $\lambda_c$. Another constitutive parameter is more commonly used: the work of separation per unit area, or fracture toughness, $G_c$ $(J/m^2)$. It is defined as the

integrand of the traction-displacement curve (see Figure 7).

$$G_c = \int_0^{+\infty} \tau(\lambda) d\lambda = exp(1)\tau_{max}\lambda_c \tag{14}$$

These parameters can be measured experimentally. When the CZE is loaded, its behavior follows the exponential curve. But when the CZE is unloaded, the TSL is modified to represent the damaging of the bound. An new elastic (un)loading path is defined by equation (15).

$$\tau = K(1 - D)\lambda \tag{15}$$

K is the virgin stiffness and D the damage variable, increasing from 0 for the undamaged state to 1 when there is no adhesion anymore.

$$K = \frac{\tau_{max}}{e\lambda_c} = \frac{G_c}{\lambda_c^2} \tag{16}$$

$$D = 1 - exp(-Q) \tag{17}$$

Q is a history variable reminding the maximal value reached by the variable $\lambda$. It satisfies Kuhn-Tucker conditions:

$$\begin{cases} (Q - \lambda) \geqslant 0 \\ \dot{Q} \geqslant 0 \\ \dot{Q}(Q - \lambda) \geqslant 0 \end{cases} \tag{18}$$

A further loading will be linear, until the exponential curve is reached (see Figure 7).

### *2.3 Some other dissipative mechanisms*

Several dissipative mechanisms are occurring near the interface at the microscopic level [27]. Because of these mechanisms, a higher amount of energy is required for the complete decohesion. The dissipated energy contributes here to improve the macroscopic adhesion. They also explain the dependency of the toughness on the mode angle since they are more pronounced in mode II. For this reason, the adhesive force will be represented in the future models with a shear to normal ration equal to one. We will study the influence of the plasticity in the metal and the friction at the interface. In this section, we will also present the concept of adhesive-cohesive failure, but it will not be investigated in this thesis.

### 2.3.1 Elasto-plastic behavior of the metal [20]

Under uniaxial loading, the behavior of an elasto-plastic material can become non linear when the applied stress $\sigma$ overcomes the elastic limit or yield stress, $\sigma_y$. Beyond this point, the slope of the stress-strain curve is lower. When the applied stress is larger than the yield stress, a permanent plastic strain $\epsilon_p$ is then created. The original piece-wise linear unloading path is then moved, as described in figure 8, but still keeps the same slope. The total strain can then be decomposed in two parts:

$$\epsilon_{tot} = \epsilon_e + \epsilon_p \tag{19}$$

Here, $\epsilon_{tot}$ is the total strain and $\epsilon_e = \frac{\sigma}{E}$ the elastic strain, with E the young modulus. It is the plastic deformation which is at the origin of the energy dissipation.

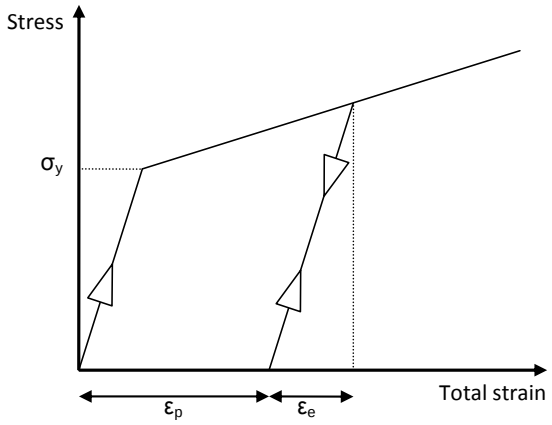


Figure 8: Elasto-plastic behavior: stress-strain curve for uniaxial loading

Under combined stress directions, a plasticity criterion is used to determine whether the behavior is still elastic or not. Several yield criteria can be used, the most popular being Tresca and von Mises criteria, respectively described in equations (20) and (21). In this formulation, the subscripts I, II and III refer to the principal components of the stress tensor.

$$max_{i \neq j} |\sigma_i - \sigma_j| \leqslant \sigma_e \qquad i, j \in \{I, II, III\} \tag{20}$$

$$\frac{1}{\sqrt{2}} \sum_{i \neq j} (\sigma_i - \sigma_j)^2 \leqslant \sigma_e \qquad i, j \in \{I, II, III\} \tag{21}$$

### 2.3.2 Friction at the interface [23]

Friction at this interface will be modeled using a Coulomb model. Here, the friction stress $\sigma_f$ is proportional to the normal stress $\sigma_n$ to the interface and opposed to the relative movement of the two layers. Two configurations are possible: a "stick" and a "slick" configuration. In the first one, the Coulomb stress is sufficient to prevent the relative movement of the two layers. In the second, the limit stress value is reached and limits the relative sliding.

$$|\sigma_f| \leqslant \mu\sigma_n \tag{22}$$

Here, $\mu$ is the friction coefficient. Since the transition from the "stick" to the "slick" configurations cause discontinuities that are difficult to solve numerically, a bilinear model is used as an approximation for the transition zone. Here is how this method has been implemented in the FEM software used for this work (see figure 9). The friction stress evolution is based on the incremental value of the tangential displacement of the layers in contact, $\Delta u_t$. The "stick" and "slick" configuration are respectively related to reversible and irreversible relative displacements. The behavior is the same as the behavior of elastic perfectly plastic materials. The maximum stress value is reached when the relative displacement is beyond a threshold value $\delta$. Afterwards, when the relative displacement decreases, the friction force is also reduced proportionally.

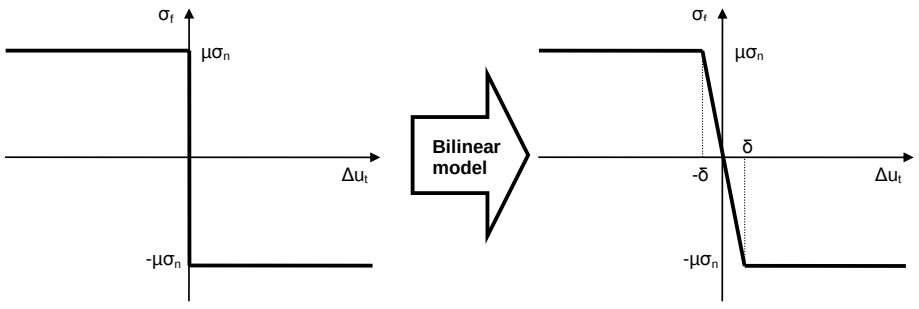


Figure 9: Representation of the Coulomb friction

### 2.3.3 A cohesive-adhesive roughness model

The delamination process does not consist in the simple separation the two considered layers at the interface only. After its initiation at the interface, a crack is able to propagate

in the weaker material. This phenomenon is called crack kinking and helps improving the toughness of the bound between the metal and the polymer because the crack propagation in the bulk material dissipates more energy than along the interface. It has been investigated in [35, 24] for a metal-polymer interface. Indeed, the macroscopic delamination process consists of a combination of adhesive (at the interface) and cohesive (in the bulk materials) failures. This process, still under investigation, is difficult to model because of the softening in the polymer which results in severe numerical issues when implemented in a finite element code. For this reason, this mechanism will not be investigated in this thesis. It will still be explained in this section as information.

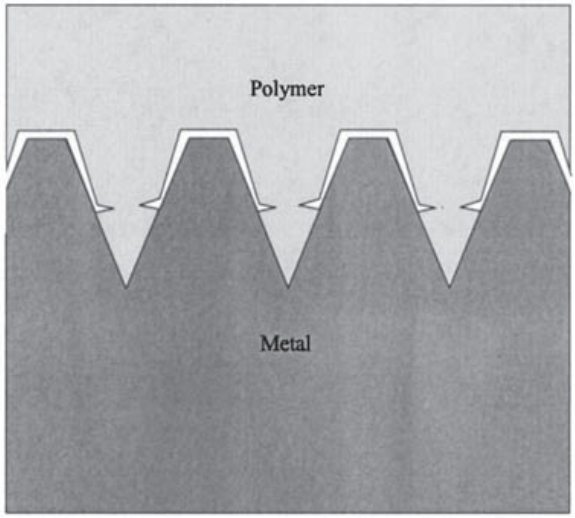


Figure 10: Adhesive and cohesive failures on a simplified interface [35]

When separation is starting between the two layers, the assumption is made that the crack initiation occurs at the interface, due to the lower value of the interface strength. Griffith's theory can be used to decide whether it propagates or not:

$$G_i \geqslant G_{ic} \tag{23}$$

where the subscript "i" stands for interface. The energy release rate $G_i$ represents the amount of energy available for the crack propagation. It includes the effects of the loading, its position with respect to the crack tip and also captures geometric parameters. It is compared to the ability of resisting to the crack growth, the fracture toughness $G_{ic}$. During the propagation along the interface, the point where crack kinking will occur is determined

using an energy released rate based criterion:

$$\begin{aligned} G_R = \frac{G_i}{G_p} > \frac{G_{ic}}{G_{pc}} \qquad &\Rightarrow \text{ interfacial cracking} \\ G_R = \frac{G_i}{G_p} < \frac{G_{ic}}{G_{pc}} \qquad &\Rightarrow \text{ bulk cracking} \end{aligned} \tag{24}$$

Where $G_i$ and $G_p$ are the interface and polymer energy release rate of the interface and the polymer, $G_{i,c}$ and $G_{p,c}$ are the interface and polymer toughness.

# CHAPTER III

## DERIVATION OF THE MACROSCOPIC TRACTION

Several benchmark are available to extract adhesive properties from bounded materials. They can be easily implemented using a finite element software in the case of a planar interface. The main difficulty is that in the case of this study, these benchmarks should also include the roughness and all the dissipative mechanisms described in the previous chapter, which occur at the micro-scale. The FEM models would require an incredibly large number of elements and very long computational times. The homogenization method provides a mean to prevent this problem. The principle is to read the interface behavior on a small portion to extract global properties that can be used at a wider scale.

Homogenization methods are widely used to obtain mechanical properties of heterogeneous materials. For instance, analytical homogenization works have been done in this way by Eshelby, Hashin, and Strikmann [15]. In our case, because of the non linearity of the dissipative mechanisms and the complexity of the geometry from the roughness representation, numerical homogenization will be used. Here, the behavior of the overall structure is calculated via a finite element model representing a small part of the structure only. This small part is called Representative Volume Element (RVE). This thesis aims at providing a homogenization method for a rough interface. The method will then be tested for a metal-polymer interface with different dissipative mechanisms such as the plasticity in the metal layer and the friction at the interface. Although it contributes to the macroscopic adhesion, the failure in the polymer will not be considered here, because of numerical issues during the resolution. As a simplification, a linear elastic behavior will be used for the polymer. The microscopic adhesion will be modeled by CZE, having the same response under shear or normal loading.

The principle of the homogenization method proposed here is to capture the traction-separation curve of the rough interface using the RVE. As a simplification, the roughness

profile is assumed to be perfectly periodic. In this case, enough information can be found in a RVE containing only a period of the roughness profile. This kind of RVE is also called unit cell [19]. The difficulty is to choose the right boundary conditions, so that the RVE behaves in the same manner as it would inside the actual structure. A method must then be set up to capture the traction-separation curve.

The following development has been inspired by several cases of interface properties homogenization. Most of these articles deal with homogenization of heterogeneous adhesives [1, 11, 10, 21, 30, 29, 34]. It is interesting to compare these cases to our in the sense that the short area surrounding the roughness profile could be considered as a heterogeneous adhesive layer.

### *3.1 The macro and the micro scales*

The homogenization method implies a multi scale description of the interface. The distinction is made between the macro and the micro scales, as depicted in Figure 11. Their description has been inspired from [1, 34].

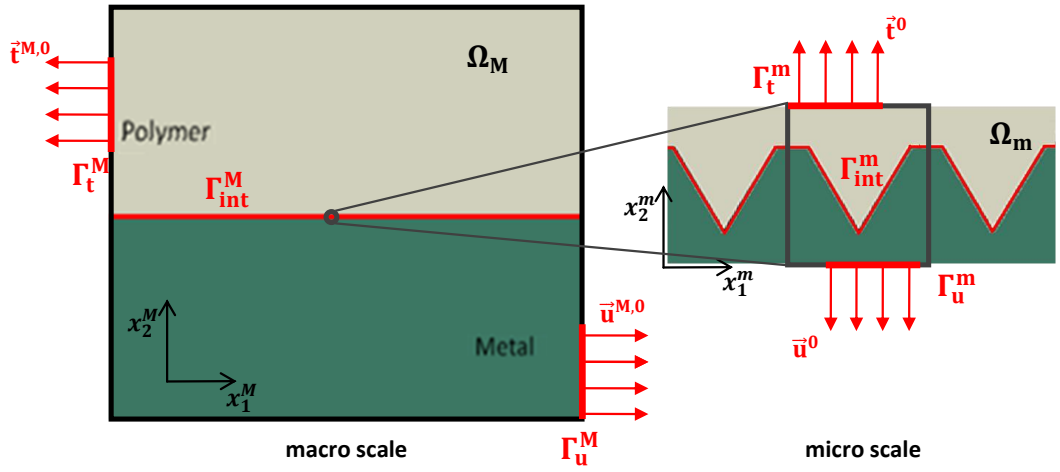


Figure 11: The macro and the micro scales

At the macro scale, a domain $\Omega_M$ is considered, with traction and displacement boundary conditions $\vec{t}^{M,0}$ and $\vec{u}^{M,0}$ respectively over boundaries $\Gamma_t^M$ and $\Gamma_u^M$. The interface $\Gamma_{int}^M$

is considered straight. The equilibrium equations at a point M located at the interface read:

$$\begin{cases} \sigma^M_{ij,j}(M) = 0, & M \in \Omega_M \\ \sigma^M_{ij}(M) n_j(M) = t^{M,0}_i(M), & M \in \Gamma^M_t \\ u^M_i(M) = u^{M,0}_i(M), & M \in \Gamma^M_u \\ \sigma^M_{ij}(M) n_j(M) = t^{M,0}_i(M), & M \in \Gamma^M_{int} \end{cases} \tag{25}$$

$\sigma^M_{ij}$ represents the term of the macroscopic stress tensor, and $u^M_i$ is the term of the macroscopic displacement. Here, the body forces have been neglected. Furthermore, the interface can be considered as an external boundary. The fourth line in (25) is a result of the equilibrium equations considering the interface as an external boundary. Applying the principle of virtual displacements under small strain hypothesis leads to:

$$\int_{\Omega^M} \sigma^M_{ij} \delta\epsilon^M_{ij} d\Omega^M + \underbrace{\int_{\Gamma^M_{int}} t^M_i \delta[\![u^M_i]\!] d\Gamma^M_{int}}_{\delta W^M_{coh}} = \int_{\Gamma^M_t} t^M_i \delta u^M_i d\Gamma^M_t \tag{26}$$

Here, $[\![u^M_i]\!]$ represents the macroscopic displacement jump across the interface, $\delta W^M_{coh}$ the cohesive work at the interface.

For each point M belonging to the interface at the macro scale is assigned a micro domain $\Omega_m$ subjected to traction and displacement boundary conditions $\vec{t}^0$ and $\vec{u}^0$ respectively over boundaries $\Gamma^m_u$ and $\Gamma^m_t$. The interface $\Gamma^m_{int}$ is represented with its roughness profile. Similar to (25) and (26), equilibrium equations and the principle of virtual displacements read:

$$\begin{cases} \sigma^m_{ij,j}(M) = 0, & M \in \Omega_m \\ \sigma^m_{ij}(M) n_j(M) = t^0_i(M), & M \in \Gamma^m_t \\ u_i(M) = u^0_i(M), & M \in \Gamma^m_t \\ \sigma^m_{ij}(M) n_j(M) = t^0_i(M), & M \in \Gamma^M_{int} \end{cases} \tag{27}$$

$$\int_{\Omega^m} \sigma^m_{ij} \delta\epsilon^m_{ij} d\Omega^m + \int_{\Gamma^m_{coh}} t^m_i \delta[\![u_i]\!] d\Gamma^m_{int} = \int_{\Gamma^m_t} t^m_i \delta u_i d\Gamma^m_t \tag{28}$$

$\sigma^m_{ij}$ represents the term of the microscopic stress tensor, $u_i$ and $t_i$ are the terms of respectively the microscopic displacement and the microscopic traction.

The link between the macro and the micro scales can be shown in separating the microscopic displacement field in two components:

$$u_i(x_j^M, x_k^m) = u_i^M(x_j^M) + \tilde{u}_i(x_k^m) \tag{29}$$

$\tilde{u}_i$ represents the displacement fluctuations due to the roughness profile at the micro scale.

### *3.2 Definition of the Representative Volume Element (RVE)*

Let us recall that the aim of this homogenization method is to capture the macroscopic traction-displacement evolution of the interface, which is the macroscopic response incorporating the microscopic adhesion forces, the effect of the roughness profile and all the other dissipative mechanisms when the two considered layers are debounding. As explained previously, we assume a periodic roughness profile. This allows to model only one period of the roughness profile in the RVE built from the mean roughness values. For the RVE to be representative of the actual interface, the right boundary conditions have to be chosen to mimic the presence of the surrounding material. To achieve this, the left and right sides of the unit cell are subjected to periodic boundary conditions to take in account the repeatability of the structure along the horizontal direction. These periodic boundary conditions remain an approximation. Indeed, they assume a periodicity of the displacements and stress fields, and in this way, they do not allow the representation of a crack propagating along the interface. But in this case, this approximation is not penalizing since we are more interested in the evolution of the macroscopic adhesion forces (macroscopic traction separation law of the interface) than in describing the crack propagation itself. On the top and bottom sides, the loading is applied in a rigid way, which means that the edges are constrained to remain straight. These boundary conditions are depicted in figure 12. They have been also used in other works on the homogenization of heterogeneous adhesives [29, 11, 10, 34]. The global mode angle is defined as $\theta = Arctan(\frac{v}{w})$ [29, 11]. The superscripts L, R, B and T stand to refer to the vectorial quantities on respectively the left, right, bottom or top border of the unit cell.

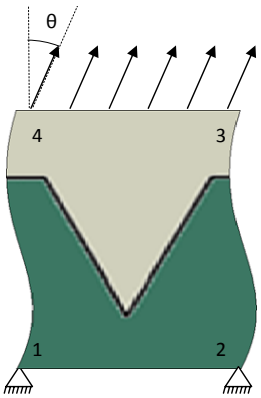


$$\begin{cases} u_i^B = 0 \\ u_i^T = v.\delta_{i1} + w.\delta_{i2} \end{cases}$$
$$i \in \{1, 2\}$$

Figure 12: The unit cell for mode angle $\theta$

Furthermore, [1] proposed another set of boundary conditions labeled as "case 2" in Figure 13 which allows to both layers in the RVE to compress or expand during the loading. However, in our model, for a non normal loading , i.e. $\theta \neq 0$, this set of boundary conditions cannot really be implemented in the FEM model because the two components of the displacement are already imposed on the top side, which means that the eventual dilatation or expansion of the top layer is not possible anymore. It can still be easily applied for normal loading by imposing only a normal displacement on the top side. Further investigations will be done in order to find which boundary condition case can lead to the most accurate effective properties after computation.

Considering $\tilde{u}$, the displacement fluctuation defined in 29, the periodic boundary conditions can be formulated as:

$$\begin{aligned} \tilde{u}_i^L(s) &= \tilde{u}_i^R(s) \\ t_i^L(s) &= -t_i^R(s) \end{aligned} \tag{30}$$

Here, $s$ is the local coordinates along the vertical sides of the RVE. The displacement fluctuations are constrained to be identical on the left and right sides. The equations related to the tractions ensure the total work of the periodic boundary conditions to be equal to zero. In this configuration, the displacements of the four nodes on the corners correspond to the macroscopic displacement. The displacement jump across the adhesive layer can be expressed by:

$$[\![u_i^M]\!] = u_i^{M,T} - u_i^{M,B} = u_i^4 - u_i^1 = u_i^3 - u_i^2 \tag{31}$$

The periodic displacement boundary conditions can then be written as:

$$\begin{aligned} u_i^R(s) &= u_i^L(s) + u_i^2 - u_i^1 \\ &= u_i^L(s) + u_i^3 - u_i^4 \end{aligned} \tag{32}$$

An alternative to the use of periodic boundary conditions could be the so-called minimal kinematic boundary conditions, which are used in [22, 12] for a unit cell including inhomogeneities. The uniqueness of the solution has been already proven for linear problems. These boundary conditions don't require a symmetric mesh and could be used to simulate non symmetric crack growth. Their disadvantages are that they don't perform very well when the inhomogeneities are close to the border. They won't be tested in this study because of the complexity of their implementation, but it could be interesting to explore this way in further works.

In the case of mode I loading, the unit cell model can be simplified. Since the loading is symmetric, if the roughness profile is symmetric as well, half of the unit cell only can be represented. In this case, the horizontal displacement is suppressed on the sides of the unit cell (see Figure 13).

### *3.3 Derivation of the macroscopic traction*

The determination of the traction is based on Hill's lemma on average work [9], which states that the average work at the micro scale is equal to the work of the average stress and the average strain over the unit cell [1]. That allows writing:

$$\overline{\delta W^m} = \delta w_{coh}^M, \qquad \text{with } \delta w_{coh}^M = t_i^M \delta [\![ u_i^M ]\!] \tag{33}$$

The average virtual work at the micro scale can be written using the principle of the virtual work under small deformation assumption:

$$\overline{\delta W^m} = \frac{1}{b} \int\limits_{\Gamma_t^m} t_i \delta u_i d\Gamma_t^m = \frac{1}{b} \left( \int\limits_{\Gamma_t^m} t_i \delta u_i^M d\Gamma_t^m + \int\limits_{\Gamma_t^m} t_i \delta \tilde{u}_i^M d\Gamma_t^m \right) \tag{34}$$

where $\Gamma_t^m$ is the boundary for the traction boundary conditions and $b$ the thickness of the unit cell.

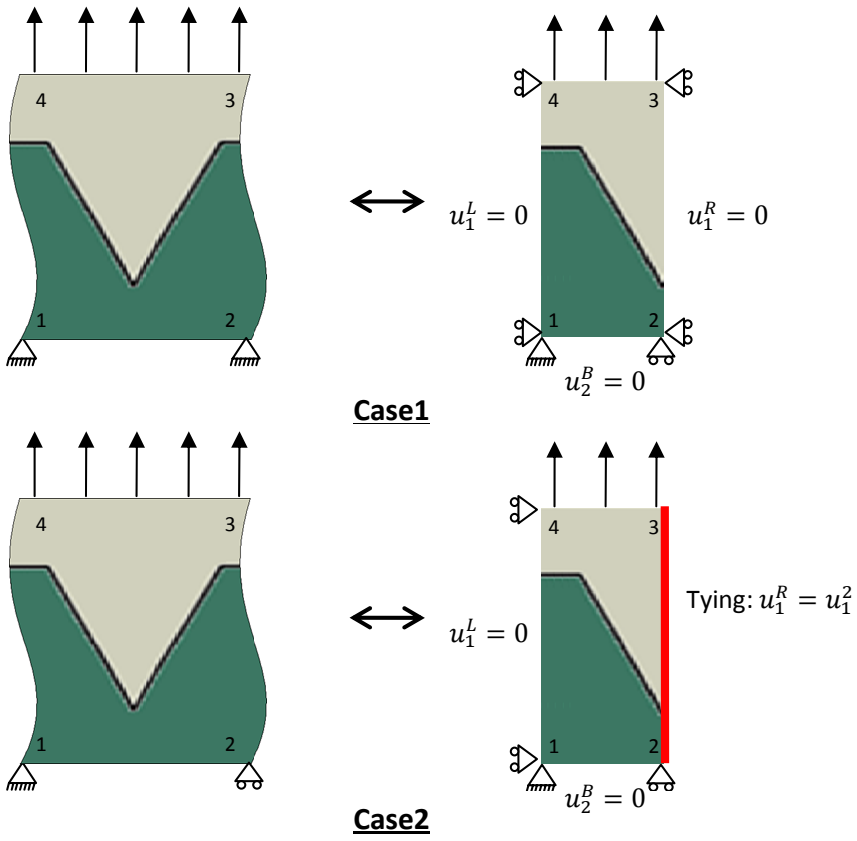


Figure 13: The two sets of boundary conditions and the simplification of the RVE for normal loading based on the symmetry of the model

Using the periodic and rigid boundary conditions on the edges of the unit cell leads to the nullification of the second integrand in equation (34). On the other hand, the integrand including the macroscopic displacement can be simplified to:

$$\int_{\Gamma_t^m} t_i \delta u_i^M d\Gamma_t^m = \int_{\Gamma_L^m} t_i^L \delta u_i^{M,L} d\Gamma_L^m + \int_{\Gamma_R^m} t_i^R \delta u_i^{M,R} d\Gamma_R^m + \int_{\Gamma_B^m} t_i^B \delta u_i^{M,B} d\Gamma_B^m + \int_{\Gamma_T^m} t_i^T \delta u_i^{M,T} d\Gamma_T^m \quad (35)$$

### 3.3.1 Case 1 of boundary conditions

We will establish the macroscopic traction vector in the case of any loading mode for the case 1 of boundary conditions.

Let us have a look at the integrands over the left and right sides of the unit cell in

equation (35). From the definition of the periodic boundary conditions in (30) and (32), we have:

$$\int_{\Gamma_t^m} t_i^R \left( \delta u_i^{M,R} - \delta u_i^{M,L} \right) ds = \left( \delta u_i^2 - \delta u_i^1 \right) \int_{\Gamma_t^m} t_i^R ds \tag{36}$$

For case 1, the loading on the upper and lower sides is such that the displacement of vertice 1 and 2 is null: the integrand (36) vanishes.

The integrands over the top and bottom sides in (35) will now be investigated. Since the bottom of the unit cell is clamped, the integrand over $\Gamma_B^m$ is equal to zero. The integrand (35) becomes:

$$\int_{\Gamma_t^m} t_i \delta u_i^M d\Gamma_t^m = \int_{\Gamma_T^m} t_i^T \delta u_i^{M,T} ds = \delta u_i^4 \int_{\Gamma_T^m} t_i^T ds \tag{37}$$

The displacement term can be replaced by the displacement value at node 4 and then extracted from the integrand thanks to the displacement boundary conditions on the top side. Using (33), the fact that $u_i^1 = 0$, (34), (35) and (37) imply:

$$t_i^M \delta [\![ u_i^M ]\!] = t_i^M \delta u_i^4 = \frac{1}{b} \delta u_i^4 \int_{\Gamma_T^m} t_i^T ds \tag{38}$$

The macroscopic traction can then be expressed as the average microscopic traction over the upper side of the unit cell.

### 3.3.2 Case 2 of boundary conditions

Here, we are only developing the calculations for the normal loading. Similarly to case 1, equation (36) can be written using the periodic boundary conditions. The definition of the boundary conditions for case 2 reads:

$$\begin{cases} \delta u_1^1 = \delta u_2^1 = 0 \\ \delta u_2^2 = 0 \\ \displaystyle\int_{\Gamma_R^m} t_1^R d\Gamma_R^m = 0 \end{cases} \tag{39}$$

The possibility of the unit cell to contract or expand in $x_1^m$ direction implies the average traction equals zero in this direction. In the end, the integrand in (39) disappears.

The integrands over the top and bottom sides in (35) give:

$$\begin{aligned}
&\int_{\Gamma_T^m} t_i^T \delta u_i^{M,T} ds + \int_{\Gamma_B^m} t_i^T \delta u_i^{M,B} ds \\
&= \int_{\Gamma_T^m} t_1^T \delta u_1^{M,T} ds + \int_{\Gamma_T^m} t_2^T \delta u_2^{M,T} ds + \int_{\Gamma_B^m} t_1^T \delta u_1^{M,B} ds + \int_{\Gamma_B^m} t_2^T \delta u_2^{M,B} ds \\
&= \int_{\Gamma_T^m} t_2^T \delta u_2^{M,T} ds + \int_{\Gamma_B^m} t_2^T \delta u_2^{M,B} ds \\
&= \int_{\Gamma_T^m} t_2^T \delta u_2^{M,T} ds
\end{aligned} \tag{40}$$

The integrands in the $x_1^m$ direction vanish because the displacement is let free in this direction. Moreover, the displacement on the $x_2^m$ direction is forbidden on the bottom side. Equation (35) becomes:

$$\int_{\Gamma_t^m} t_i \delta u_i^M d\Gamma_t^m = \int_{\Gamma_T^m} t_2^T \delta u_2^{M,T} ds = \delta u_2^4 \int_{\Gamma_T^m} t_2^T ds \tag{41}$$

Then, combining (33), (34), (35) and (41) leads to:

$$t_i^M \delta [\![ u_i^M ]\!] = \frac{1}{b} \delta u_2^4 \int_{\Gamma_T^m} t_i^T ds \tag{42}$$

Since vertex 1 is clamped and the unit cell is subjected to normal loading, the displacement jump is equal to the vertical displacement of vertex 4. Finally, the expression of the macroscopic traction is valid for case 1 for any loading mode and for case 2 for normal loading:

$$t_i^M = \frac{1}{b} \int_{\Gamma_T^m} t_i^T ds \tag{43}$$

# CHAPTER IV

# NUMERICAL IMPLEMENTATION

## *4.1 Extraction of the macroscopic TSL*

The homogenization method is applied with a Korn shell script on Unix OS (see figure 14). The first goal of this script is to create parametric models allowing a variation of the geometry and mesh, which is not directly feasible in the commercial package. First, the parameters of the finite element model are entered in a format compatible with the procedure file format used by the finite element modeler, Mentat, to build the model. These parameters include the geometry, mesh size, material properties, and the resolution option. Then, depending on the chosen options, the right procedure file is assembled and used in the modeler to create a model readable by the solver. In a second time, some other options that cannot be directly included using the procedure file are added using several sub scripts. They primarily deal with the creation of servo links, which can be used, for instance, to generate the periodic boundary conditions. This final model is then submitted to the solver, MARC, and two output files are generated. The first one is a post-processing file, which can be read with the post-processing component of the modeler to check the deformation of the RVE during the simulation. Several output values can be investigated, such as the deformed shape, the stress or strain fields, the damage values in the cohesive zone, etc. The second file contains the values of displacement and reaction force at the constrained node of the unit cell, named "vertex 4" in figure 12. This file is imported in Matlab to draw the traction-displacement curve and extract the homogenized values.

For a given mode angle, three cohesive parameters are identified. The interface toughness $G_c$ is computed as the integrand below this curve, which is computed using the trapeze method. Here, $N$ is the number of recorded points.

$$G = \sum_{i=1}^{N-1} \frac{(\delta_{i+1} - \delta_i)(\tau_{i+1} - \tau_i)}{2} \tag{44}$$

The interface strength $\tau$ corresponds to the maximum traction, and the corresponding

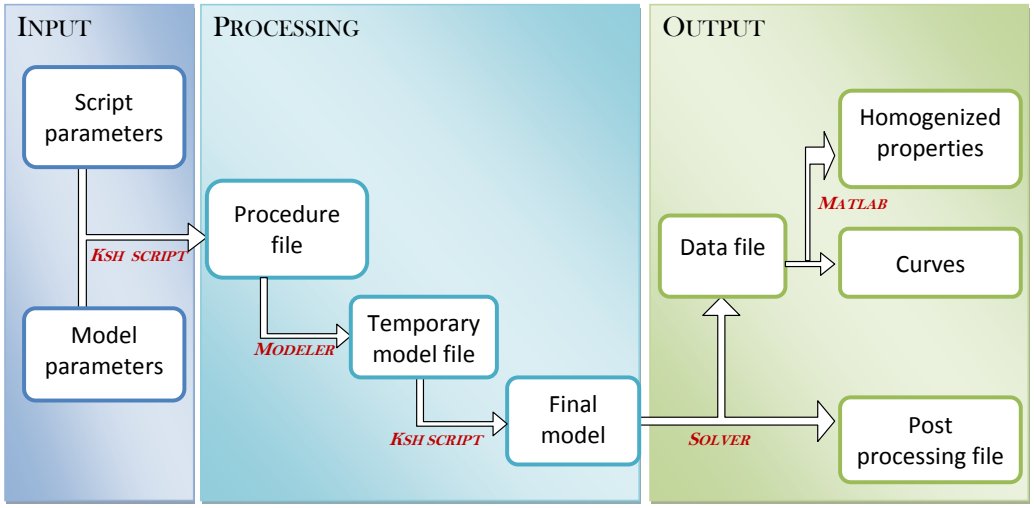


Figure 14: The homogenization script

displacement value is recorded as the critical displacement value. The homogenized interfacial properties values can then be used in a macroscopic TSL. Here, we choose to use an exponential law, as described in equation (13), using the toughness and the strength values only. The error between the fitted (subscript $fit$) and the experimental TSL (subscript $sim$) is expressed proportionally to the strength value to allow comparison between different curves.

$$error = \frac{1}{N}\sum_{i=1}^{N}\frac{|\tau_{sim,i} - \tau_{fit,i}|}{\tau_{sim,max}} \tag{45}$$

This script has been tested for a flat interface between two identical elastic materials. In order to capture the separation of the interface, the interface strength value must be small enough that elongation in the bulk material may be neglected. For this reason, two kinds of results can be observed, as depicted in figure 15. In the test 1 depicted in figure 15a, the strength is set up at 10.34 MPa with a Young modulus of 126,000 MPa for the elastic material. When the load is applied, the CZE is damaged before the bulk material is deformed. The homogenized traction separation law in this case only captures the original TSL of the RVE. On the other hand, test 2, as shown in figure 15b, does not allow a direct reading of the TSL of the interface. Here, the same value is used for the interface strength, but the stiffness is reduced to 500 MPa. The traction necessary to separate the layers is now such that the deformation in the bulk layers can no longer be neglected. The effect is

clearly visible in the traction-displacement curve for test 2: the exponential fitting of test 2 does not fit the experimental points as well as test 1, as reflected by the values of the error in fitting listed in table 1.

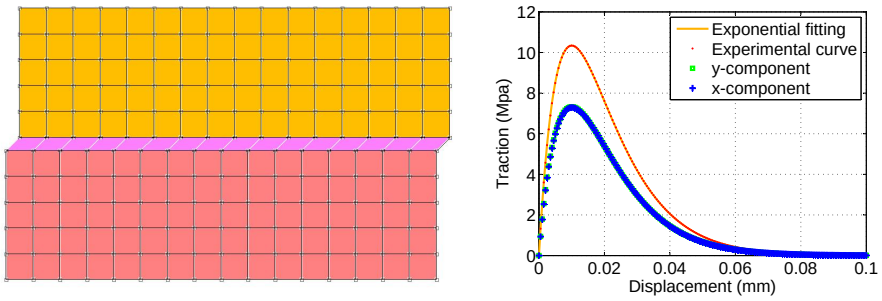


(a) Test1: Cohesive properties small with respect to the bulk material properties (E = 126,000 MPa)

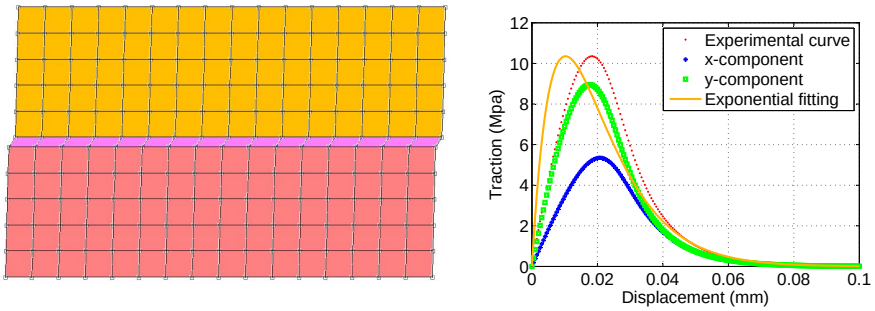


(b) Test2: Cohesive properties large with respect to the bulk material properties (E = 500 MPa)

Figure 15: The homogenization of a flat interface for a load angle $\theta = 45°$ with $t_{max}$=10.34 MPa and $G_c$=0.281 N/mm. Results listed in table 1

Table 1: CZE properties and homogenized results for a flat interface

| | Critical displacement | Strength | Toughness | Error |
|---|---|---|---|---|
| CZE | 0.01 mm | 10.34 MPa | 0.281 N/mm | |
| Test1 | 0.01 mm | 10.34 MPa | 0.2808 N/mm | 1.11 x$10^{-6}$ |
| Test2 | 0.0185 mm | 10.35 MPa | 0.2887 N/mm | 1.88 x$10^{-2}$ |

### *4.2 Reference benchmarks*

Several benchmarks are used to determine interface toughness. In this section, we focus on the Double Cantilever Beam (DCB) and the 3-point End Notched Flexure (3ENF) tests, two of the most widely documented tests for mode I and II loading. The method involves

performing a fitting of the analytical solutions of these benchmarks to the curves obtained with the numerical solution.

### 4.2.1 Double Cantilever Beam (DCB)

The interface toughness under mode I loading can be checked using DCB benchmark [4, 36]. Two layers of equal material properties and length L are bounded. An initial crack of length $a_0$ is inserted at one of the tips of the interface. In the finite element model, this crack is represented by the absence of Cohesive Zone Elements. The mode I loading at the interface is obtained by applying a vertical displacement u on the beginning of the cracked part at the extremity of both layers.

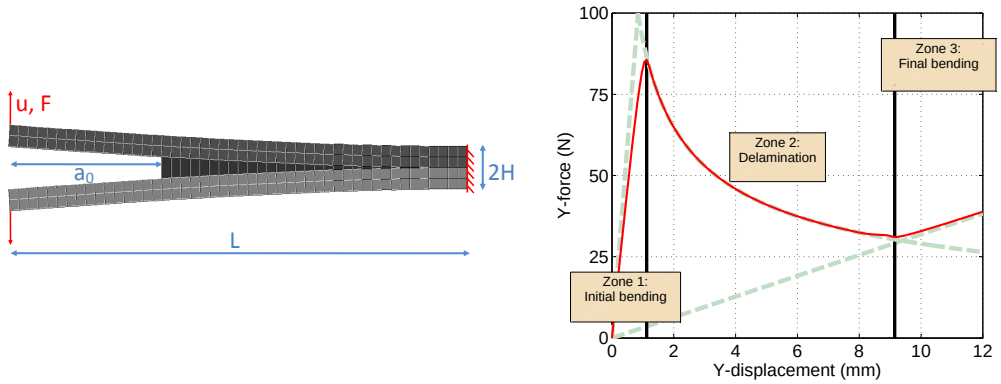


Figure 16: The Double Cantilever Beam

During the loading, the behavior of the layers can be divided in three parts, as described in figure 16. First, before the crack propagates, the DCB behaves in the same manner as a simple cantilever beam of length $a_0$ (Zone 1). Then, delamination occurs (Zone 2) until the crack reaches the end of the beam. Finally, the traction-separation curve reaches the result of a cantilever beam of length L (Zone 3).

In the following, the analytical expression of the delamination part is developed [4, 36]. The first step is to write the energy release rate, which can be expressed in terms of the change in compliance, as described by:

$$G_I = \frac{F^2}{2w}\frac{\partial C}{\partial a} \tag{46}$$

The compliance $C$ can be written using beam theory for elastic materials. $E$ is the elastic stiffness of the material.

$$C = \frac{u}{F} = \frac{a^3}{3EI} \qquad \text{with } I = \frac{wh^3}{12} \tag{47}$$

Deriving the expression of the compliance in (47) and substituting in expression (46) allows simplification of the energy release rate expression:

$$G_I = \frac{F^2 a^2}{wEI} \tag{48}$$

The expression of the compliance can also be used for expressing the crack length, $a$:

$$a = \left(\frac{3EIu}{F}\right)^{1/3} \tag{49}$$

This expression can be replaced in the expression of the energy release rate:

$$G_I = \frac{1}{wEI}\left(3F^2 EIu\right)^{2/3} \tag{50}$$

Clearly, in this experiment, the energy release rate equals the toughness value.

The DCB simulation is performed in Marc-Mentat and the reaction forces and displacement values on the loading point written in a data file. Expression (50) is evaluated for each point in the delamination part of the traction-displacement curve (see figure 17), which is assumed to be identified using the following expression:

$$u \in [u_{ds} + k_1 \ ; \ u_{de} - k_2] \tag{51}$$

Here $u_{ds}$ and $u_{de}$ are the displacement values at the start and the end of the delamination, respectively, which are determined by the change of sign of the slope of the traction-displacement curve. To avoid the transition state between the different zones, two adjustable parameters $k_1$ and $k_2$ have been included to select the portion of the curve where the numerical result fits the analytical curve best. $G_{Ic}$ is then computed as the mean value of the expression (50) for u, assuming condition (51). The stars on figure 17 represent the start and end of delamination considered for the toughness computation.

Figure 17 shows the results of the DCB test for a straight interface. The material and geometric properties used are summarized in table 2. The simulations are performed under

Table 2: Material and geometric properties of the specimens used in the benchmarks

| $L$ | $h$ | $a_0$ | $w$ | $E$ | $\nu$ | $\lambda_c$ | $G_c$ |
|---|---|---|---|---|---|---|---|
| 100 mm | 1.5 mm | 30 mm | 30 mm | 126 GPa | 0.281 | 0.01 mm | 0.281 N/mm |

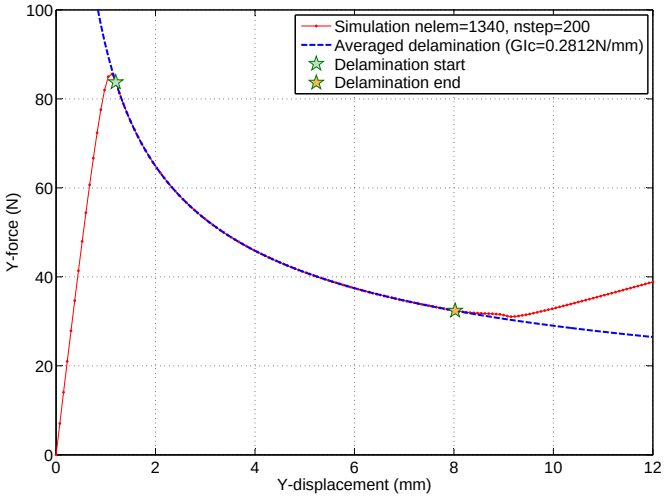


Figure 17: Traction-displacement curve for the DCB

plane strain conditions. The output is a toughness value of 0.2815 N/mm, which matches the actual toughness used for the CZE with an error of only 0.07%.

The DCB can also be used to capture the total traction-separation curve of the interface. This method is presented in [2, 16]. The inverse solution is theoretically developed in [25]: at the tip of the initial crack, the local stress value $\sigma$ can be expressed as a function of the opening $\delta_n$, the reaction force $F$, and the rotation $\alpha$ of the loaded edges of the DCB and rotation of the load using the following equation:

$$\sigma = \frac{2}{w}\frac{d(F\theta)}{d\delta_n} \tag{52}$$

This equation is then used to draw the traction-separation law of the interface from experimental results of a DCB test. In addition to the reaction force at the loaded edges, this method requires recording the evolution of $\theta$, identified as the angle between the edge of one of the layers of the DCB sample, and the opening value at the location of the initial crack tip, $\delta_{n,exp}$. From the data, the $F\theta$-$\delta_{n,exp}$ curve is drawn (figure 18a) by interpolating the simulation points with spline functions. The curve obtained is then differentiated to $\delta_n$ and multiplied by $\frac{2}{w}$ to obtain the curve of the traction-separation at the interface (figure

18b.

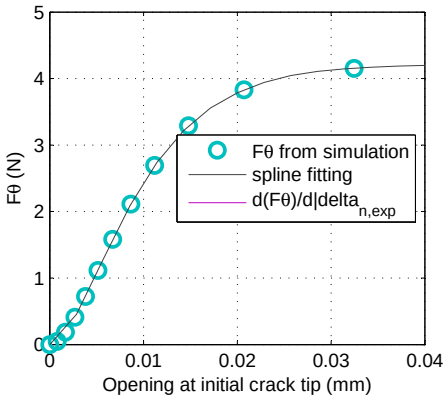


(a) $F\theta$-$\delta_{n,exp}$ curve from simulation data

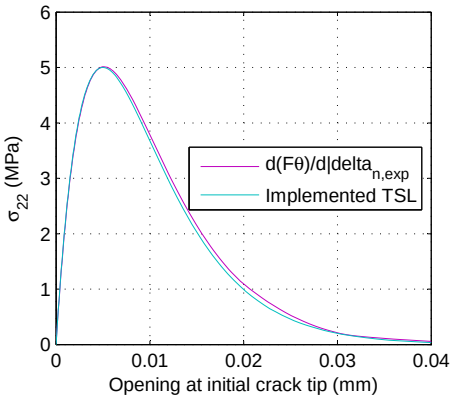


(b) Traction separation law derivate from the $F\theta$-$\delta_{n,exp}$ curve. Comparison is made with the TSL implemented in the Cohesive Zone Elements

Figure 18: Extracting the TSL using a DCB specimen

The TSL obtained illustrates that the aforementioned method can indeed be used to extract the TSL from a mode I test. However, there is a disadvantage to this method: the data used for the establishment of the TSL are taken at one point of the interface only. Therefore, the results cannot represent an entire roughness profile. This issue can be solved by capturing the average opening on a small zone around the initial crack tip.

### 4.2.2 3-point bend End-Notched Flexure test (3ENF)

The 3ENF test [4, 36, 7] is widely used to obtain experimental values of mode II toughness. Here, the two layers are bounded in a manner similar to the DCB test. The only differences are the loads and boundary conditions, illustrated in figure 19. The displacement $u$ in the center of the model is called deflection.

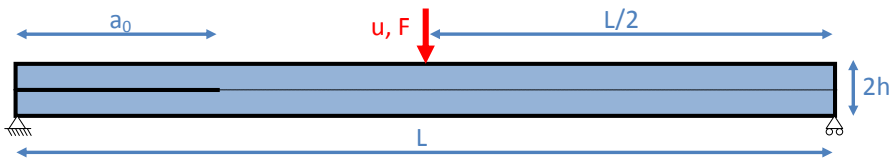


Figure 19: The 3-point bend End-Notched Flexure test

The expression for the ERR can be developed the same way as for the DCB. The expression of the energy release rate (46) based on the change of compliance is still valid. For the 3ENF, the expression of the compliance is shown below. There are two different expressions, depending on whether the crack tip is before or after the loaded point. From these expressions, the crack length is written in (54).

$$C = \frac{u}{F} = \begin{cases} \dfrac{L^3 + 12a^3}{384EI} & \text{for } a \leqslant \dfrac{L}{2} \\ \dfrac{L^3 - 3\,(L-a)^3}{96EI} & \text{for } a \geqslant \dfrac{L}{2} \end{cases} \qquad \text{with } I = \frac{wh^3}{12} \tag{53}$$

$$a = \begin{cases} \left(32EI\dfrac{u}{F} - \dfrac{L^3}{12}\right)^{1/3} & \text{for } a \leqslant \dfrac{L}{2} \\ L - \left(32EI\dfrac{u}{F} - \dfrac{L^3}{3}\right)^{1/3} & \text{for } a \geqslant \dfrac{L}{2} \end{cases} \tag{54}$$

The derivative of the compliance with respect to the crack length can be computed from (53) and then be inserted into (46). When the expression of the effective crack length in (54) is also used, one can formulate an expression for the ERR (here, for mode II):

$$G_{II} = \begin{cases} \dfrac{3F^2}{8wEI}\left(32EI\dfrac{u}{F} - \dfrac{L^3}{12}\right)^{2/3} & \text{for } a \leqslant \dfrac{L}{2} \\ \dfrac{3F^2}{64wEI}\left(32EI\dfrac{u}{F} - \dfrac{L^3}{33}\right)^{2/3} & \text{for } a \geqslant \dfrac{L}{2} \end{cases} \tag{55}$$

This energy release rate equals the fracture toughness during the delamination. The expression of $G_{II}$ for the first delamination part is used to determine the toughness value because it requires a smaller simulation time. The method used is the exact same method used to determine the $G_{Ic}$ with the DCB.

Figure 20 shows the results of the 3ENF test: the traction-displacement curve, and the evolution of the Energy Release Rate (ERR) from equation (55) for the first delamination part. The parameters used in the models are the same as the DCB (see table 2). Two values have been taken for the interface strength, 10.54 MPa (which corresponds to the initial $\lambda_c$=0.01 mm in table 2) and 80 MPa.

One can notice that the response is rather sensitive to the chosen strength: low strength correlates with experimental points too far from the analytical solution. In this situation, the ERR is not constant in the delamination zone, which can be observed from figure 20b. When $\tau_{max} = 10.54$ MPa, it is hard to identify the toughness of the interface. After

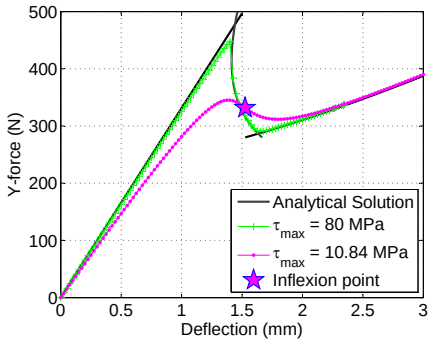


(a) Traction-displacement curve of the loaded point

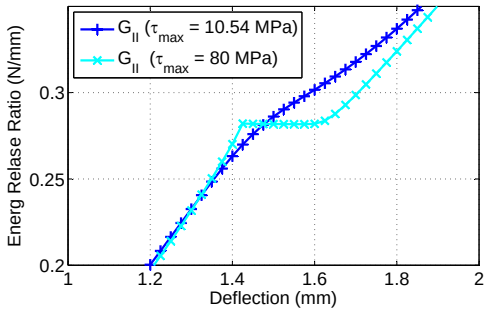


(b) Evolution of the Energy Release Rate

Figure 20: Results and post-processing for the 3ENF simulation

Table 3: Evaluation of the Energy Release Ratio for different strength values

| Strength | $G_{IIc}$ value | Error | Method |
|---|---|---|---|
| 10.54 MPa | 0.2903 N/mm | 3.3% | Inflexion point |
| 80 MPa | 0.2818 N/mm | 0.28% | Average |

comparing the toughness value implemented in the CZE with the evolution of the ERR in figure 20b, it appears that the ERR reaches the toughness value near the inflection point of the deflection-reaction curve, marked with a star on figure 20a. In this case, the toughness is evaluated as 0.2903 N/mm, with an error of 3.3%. Increasing the strength gives better results, as shown in figure 20b. For $\tau_{max} = 80$ MPa, the toughness is evaluated to 0.2818 N/mm, which results in an error of only 0.28%. One can conclude that the 3ENF is not well-adapted to capture mode II toughness when the interface strength is too low.

# CHAPTER V

# EFFECT OF A ROUGH SURFACE ON MACROSCOPIC ADHESION

This chapter presents how the tools discussed previously are used to capture the macroscopic traction-separation laws of a rough interface between two layered materials. In the first part, the simulations are performed on a model using a triangular roughness profile separating two elastic materials having the same properties. The second part explains the improvements to the model introduced to properly describe the contact between the two layers in the simulations. The third part demonstrates the results of the extraction of the macroscopic TSL for a rough interface between a copper layer and an Epoxy Mold Compound (EMC). In this last part, the effects of two dissipative mechanisms, the plasticity in the Cu and the friction at the interface, are also presented.

## *5.1 Triangular roughness profile between two identical elastic materials*

A first roughness profile has been inspired by [24] and is illustrated in figure 21. The interface is located in a way that the average height is equal in both layers. For this roughness profile, the macroscopic TSL has been computed following section 4.1 for different mode angles. These results have then been compared with the results of the DCB and 3ENF benchmarks. The decohesion is the only dissipative process considered, modeled by CZEs with $G_c = 0.281$ N/mm, $\tau = 10.34$ MPa and $\lambda_c = 0.01$mm. Elastic material is used with E = 126 GPa and $\nu = 0.263$ for both layers. The RVE is loaded with different mode angles. Because of the geometry of the roughness profile, illustrated in figure 21, two situations can be considered. When the loading angle $\theta$ is above $\theta_c$, contact constraints have to be defined to prevent the penetration of the layers. These constraints result in contact stress at the interface between the two layers, including - or not - a friction law. The influence of the friction will be investigated later in section 5.3.3. In this section, we will first present the results of a separation of the bounded layers without contact, i.e. when there is no eventual penetration to prevent, and then we will show the results when the bulk layers are deformed due to the

contact constraints.

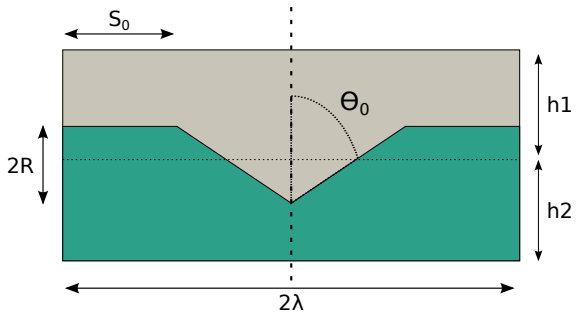


Figure 21: Geometry of the roughness profile. For this section, the values are h1 = h2 = 0.2 mm, $\lambda = 0.25$ mm, $s_0 = \frac{\lambda}{2}$, R = 0.05 mm and $\theta_c = 51°$

### 5.1.1 Separation without contact

For a loading angle $\theta < \theta_c$, the separation of the two layers only involves the damage of the adhesion force, represented by the CZE inserted at the rough interface. Here, the traction separation law of the Cohesive zone elements has a shear to normal ratio of 1. For this reason, the macroscopic traction does not depend on the shape of the roughness profile. In the model, the interface strength interface strength, 10.34 MPa, is negligible in comparison to the elastic stiffness value of the bulk layers, 126 GPa. In this case, during the delamination, the macroscopic traction required for the complete opening of the cohesive zone elements is not enough to produce a significant deformation of the bulk layers. Since the dissipative mechanisms have not been included here, the only effect of the roughness will be an increase in the contact area between the bulk layers. This increase can be easily computed as follows:

$$A_{\%} = \frac{S_0 + \sqrt{(2R)^2 + (\lambda - S_0)^2}}{\lambda} \tag{56}$$

With the actual values, the increase of area is 14%. This contact area increase will then result in an increase in the total macroscopic adhesive force on the entire RVE. The results are presented in figure 22. As explained in section 4.1, the magnitude of the macroscopic reaction stress computed from 38 is plotted with respect to the norm of the imposed displacement. From this experimental curve, the adhesive parameters are extracted (they are listed in table 4). These parameters are also used to apply an exponential fitting to the

experimental curve. The results are the same for normal loading (case1 and case2 for the boundary conditions) and for each mode angle value strictly below $\theta_c$. As expected from theory, the response still fits the exponential behavior chosen for the CZE behavior, which is confirmed by the very low value of the error between the experimental values and the exponential fitting, calculated from (45). Table 4 confirms that the macroscopic adhesive stress increases following A%.

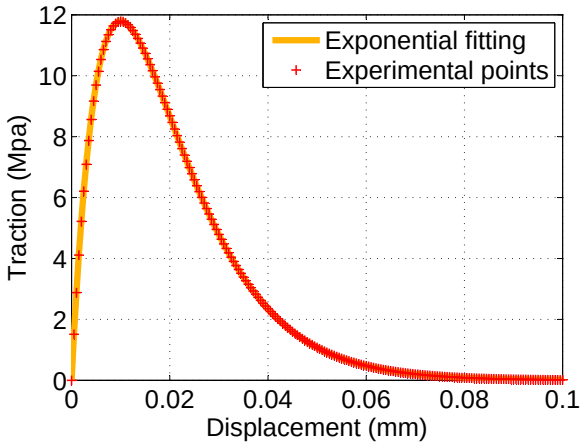


Figure 22: Traction-displacement curve for the unit cell including rough profile for $\theta < \theta_c$. The error on the exponential fitting is $1.11 \times 10^{-6}$

Table 4: Microscopic (CZE) vs. macroscopic (RVE) adhesive properties

| | Critical displacement | Strength | Toughness |
|---|---|---|---|
| CZE | 0.01 mm | 10.34 MPa | 0.281 N/mm |
| Homogenized values | 0.01 mm | 11.79 MPa | 0.3202 N/mm |
| Ratio | 1 | 1.140 | 1.140 |

To validate these results, a simulation has been performed on a DCB sample with the same rough interface. The dimensions of the geometry are the same as chosen in table 2. The output is presented in figure 23. The resulting toughness, 0.3195 N/mm, is very close to the one extracted using the homogenization method, 0.3202 N/mm.

### 5.1.2 Separation with contact

To represent the situation in which $\theta = \theta_c$, the definition of the load has been modified to allow the upper layer to "slide" on the lower one. To achieve this, the y displacement of the

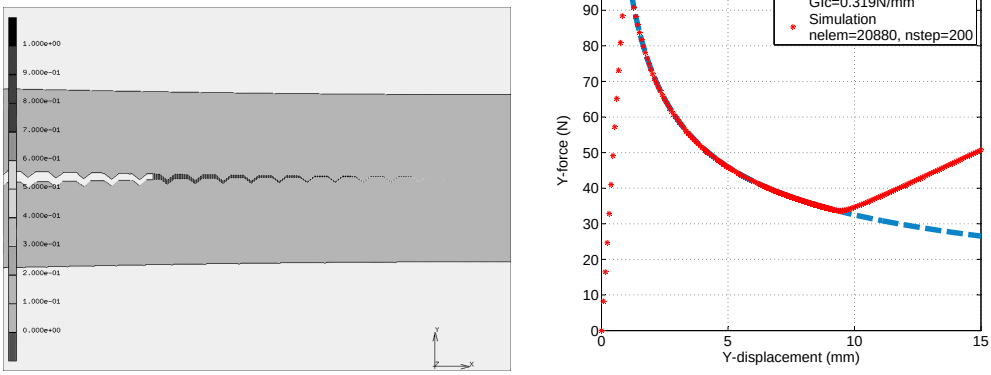


(a) Crack tip with damage in the CZEs

(b) Traction-separation curve with analytical fitting of the delamination part

Figure 23: Results of the DCB test for a rough interface

top edge of the RVE has been set free. The nodes on the top edge of the RVE are however still supposed to remain straight by tyings. The results are presented in figure 24. The same method as the previous section has been used to determine the curves. We observe that the homogenized adhesion is higher in this case than when the separation occurs without contact.

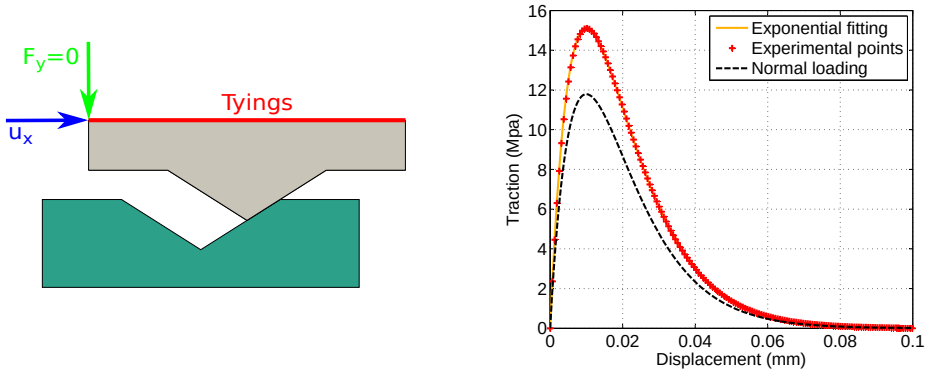


Figure 24: Separation of the layers of the RVE by "sliding" mode. The homogenized values are $G_c^M = 0.4101$ N/mm, $\tau_{max}^M = 15.11$ MPa and $\lambda_c^M = 0.01016$ mm. The TSL for normal loading is included for comparison.

Figure 25 shows the curves of the reaction stress vs. the imposed displacement. For different values of $\theta$, the graph shows the x and y components, the magnitude of the total reaction and an exponential fitting. Here, the maximum value of the displacement has been

chosen to allow a complete separation of the two layers, as illustrated by figure 26. For a loading angle greater than $\theta = Arctan\left(\frac{\lambda}{2R}\right) \approx 68°$, two periods of the roughness profile have been drawn for the lower layer to ensure the continuity of the contact.

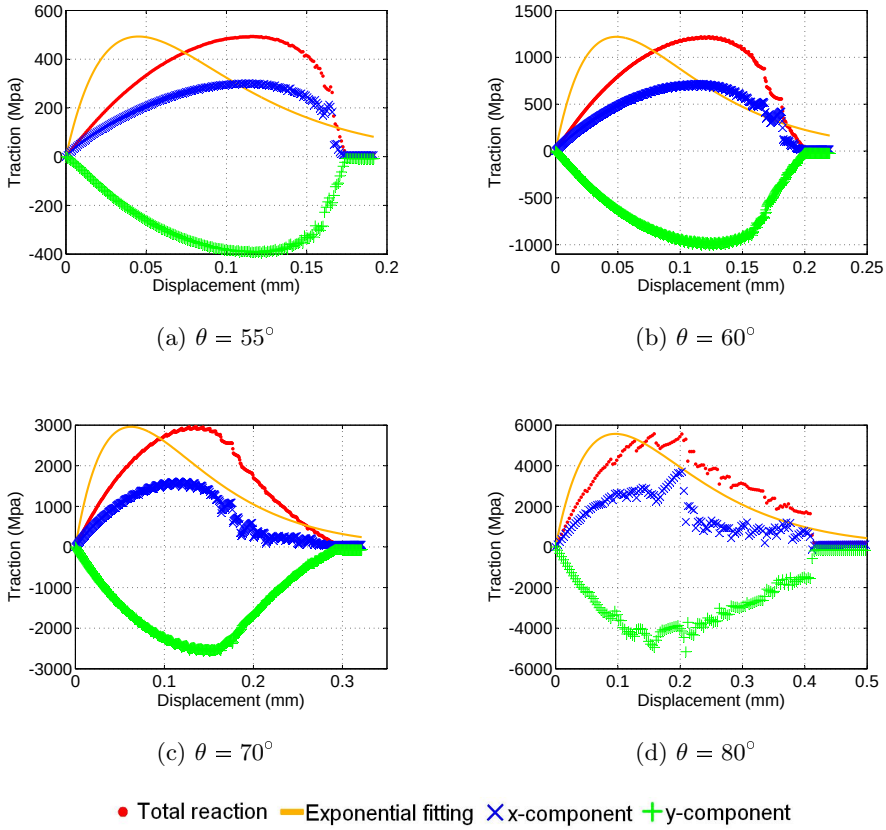


(a) $\theta = 55°$ (b) $\theta = 60°$

(c) $\theta = 70°$ (d) $\theta = 80°$

Figure 25: Traction-displacement curves – separation with contact between the bulk layers

Figure 26: Separation of the layers of the RVE

In these simulations, the layers start deforming and the bulk material behavior modifies the overall response. Since the interface strength is negligible in front of the elastic modulus of the bulk layers, the effect of the CZEs is not visible in the curves. Indeed, the computed stress values are extremely high: with a realistic material, failure would have occurred before the end of the loading path. We can observe that the response is repulsive (negative normal component of the reaction force) and that the shape of the total reaction cannot be accurately fitted using an exponential law. One can notice the oscillations in the curves.

They are resulting from a non respect of the contact between the two layers, see figure 27.

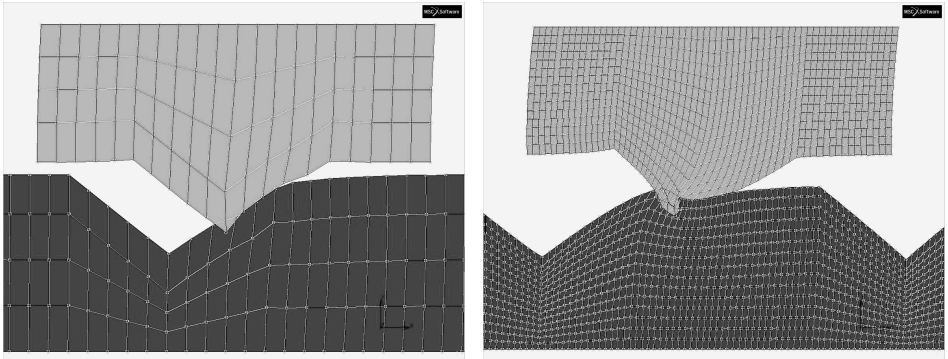

(a) Light penetration between the control nodes

(b) The nodes of the upper layer are stuck into the other one

Figure 27: Penetration issues during the collision of the two bulk layers

The contact conditions are set up with a node-based control algorithm. However, penetration can still occur between the controlling nodes, which results in some oscillations in the traction response (see figure 27a). Reducing the mesh size near the contact area can help reduce these oscillations. In the worst case, several nodes of one of the layers can become stuck inside the other layer (figure 27b), which is reflected in the traction-displacement curve by an increase in the apparent stiffness. Even if the simulation can converge, the results are not realistic at all. Reducing the time stepping during the resolution or the mesh size of the model is not enough to avoid these problems. For example, figure 28 shows the different results for a mesh refinement starting from a meshing of 4x40 elements for each layer (reference mesh size). Another model has been done from the same model to which a mesh refinement has been done at the interface (mesh size /3 at the interface). Two other simulations have been performed with meshes of respectively 8x80 (mesh size /2), 12x120 (mesh size /3) for each layers. Although the oscillation period decreases, the layers become more likely to get stuck. In short, this model does not allow the extraction of macroscopic adhesive properties.

A 3ENF test has been performed on a rough interface for the first roughness profile (see figure 29). The toughness has been computed for a CZEs having an strength of 10.34 MPa, but also for 80 MPa for validation. Indeed, it has been shown in section 4.2.2 that

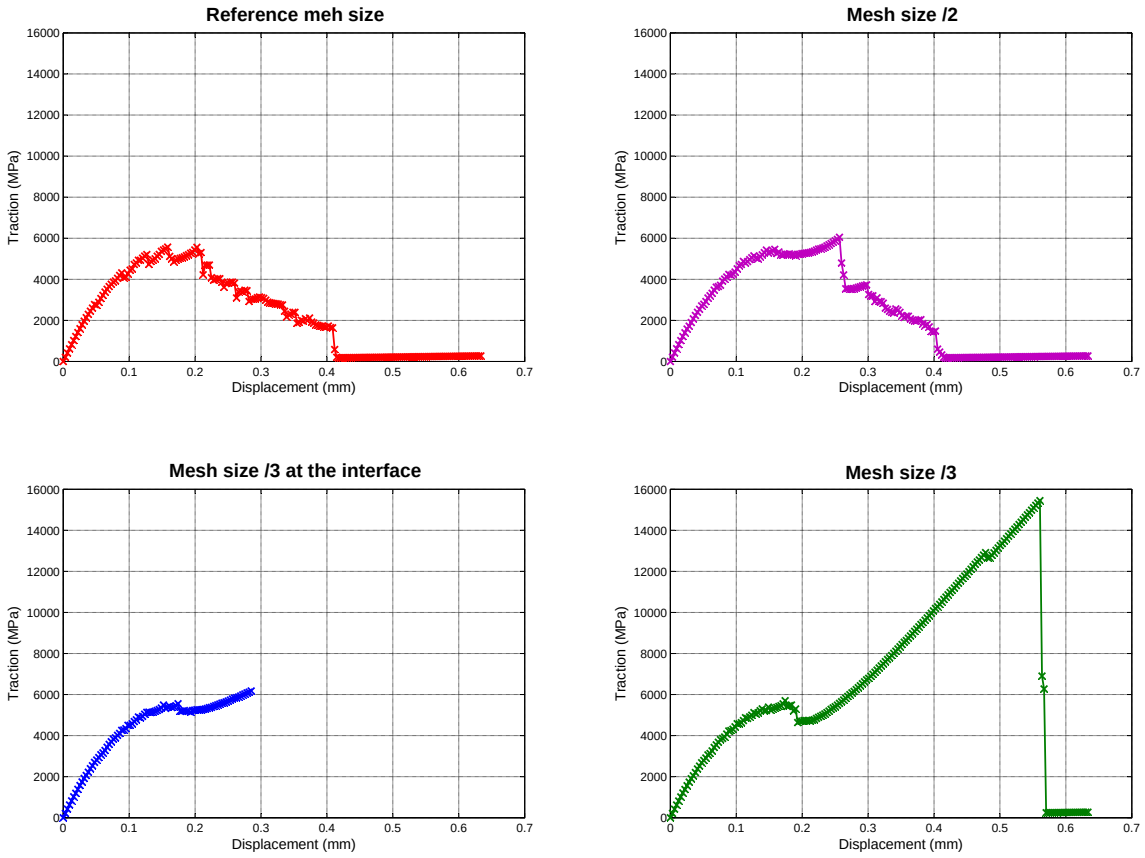


Figure 28: Effect of the mesh refinement on the traction-displacement curve. The simulations have been performed for a load angle of 80°.

the results for the 3ENF are more accurate for a higher toughness of the interface. The computed values are respectively 0.3156 N/mm and 0.3171 N/mm: the two values are close to one another, so we can consider that the results are acceptable.

Table 5 sums up the results from the RVE simulations and the benchmarks. We can see that for the chosen parameters the 3ENF and the DCB give results similar to the results of a RVE loaded with a mode angle strictly below $\theta_c$. The results for a "sliding" configuration result in higher homogenized adhesive properties.

Table 5: Computed toughness values for different simulations

| RVE: $\theta < \theta_c$ | RVE: $\theta = \theta_c$ | DCB | 3ENF |
|---|---|---|---|
| 0.3202 N/mm | 0.4101 N/mm | 0.3195 N/mm | 0.3156 N/mm |

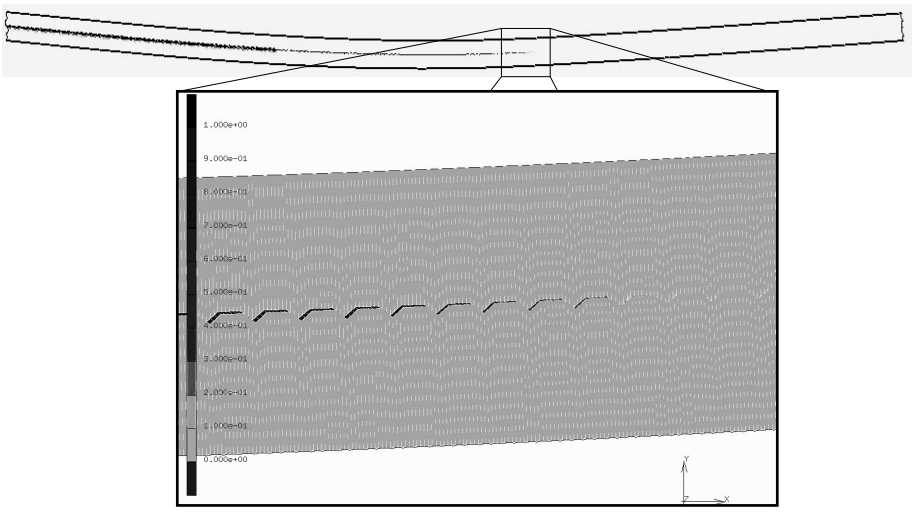

(a) Crack tip and beginning with damage value in the 3ENF

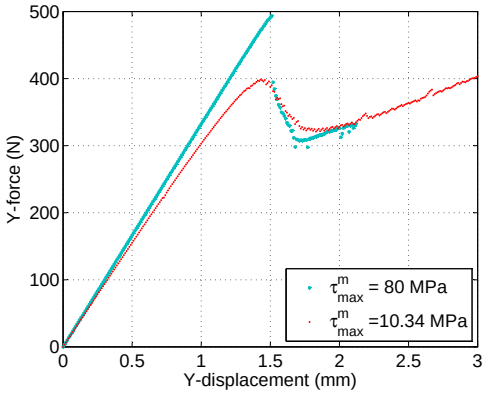


(b) Traction-displacement curve for strength values at the interface 10.34 and 80 MPa

Figure 29: Results of the 3ENF test for a rough interface

## *5.2 Contact improvement*

The simulations on the first rough profile have shown that an improvement of the contact definition is required. Let us first explain the principle of the contact algorithm used in the FEM software [23]. From the contact point of view, the two layers in the model are defined by the elements composing them, the nodes of the outside frontier which are considered as likely to contact the other layer, and the edges describing the outside border. When the two layers start touching each other, penetration is prevented by the following rule. First, the algorithm determines which layer is touching the other. Penetration is then defined

as occurring when a node of the touching layer is crossing the outside border of the other layer. To prevent this, a contact force normal to the outside border of the touched layer is applied to the penetrating node, as depicted in figure 30.

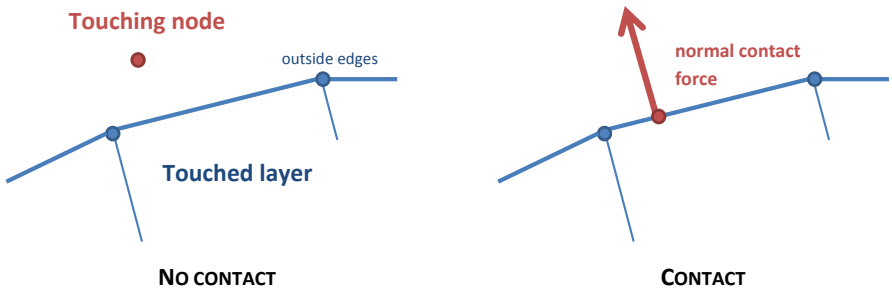


Figure 30: Definition of the contact algorithm

This explanation of the contact algorithm gives several possibilities to improve the contact between the two layers. First, one can remark that the contact would be easier to describe if the touched layer deforms less than the touching one. It is interesting for this study since the final simulations will be run for a metal-polymer interface, which implies a notable difference in stiffness for the two layers. Seconds, an interesting possibility is to change the shape of the roughness profile into a spline to facilitate the continuous determination of the normal of the touched layer. Indeed, even if the mesh at the interface seams to discretize the border, the normal at the contact can still be defined using the analytical definition of the spline. The last idea is to use a finer mesh for the touching layer, in first place because it will undergo more deformation, and also because it will help when a node of the touching layer is passing from one edge of the touched layer to the other. However, this solution may cause meshing and continuity issues for the stress fields. Due to the use of CZE at the interface, some nodes of the interface elements will have to be inserted in the edges of the elements composing the layer with the coarse mesh, see figure 31.

The above changes have been tested for a Copper - Epoxy Mold Compound (EMC) interface. The model properties are listed in table 6. The geometric values have been taken from [24]. As a simplification, an elastic behavior is used for both layers. Three kinds of models have been used. The first one uses rigid contact, where the copper layer

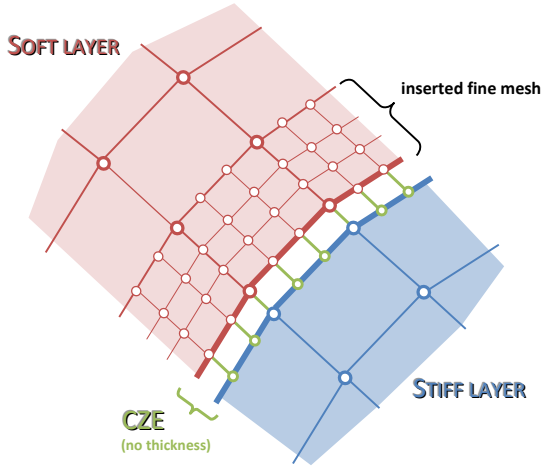


Figure 31: Mesh refinement near the interface: a finer mesh is inserted in the soft layer. Tyings are set up to have a compatible displacement field when passing from one mesh to the other.

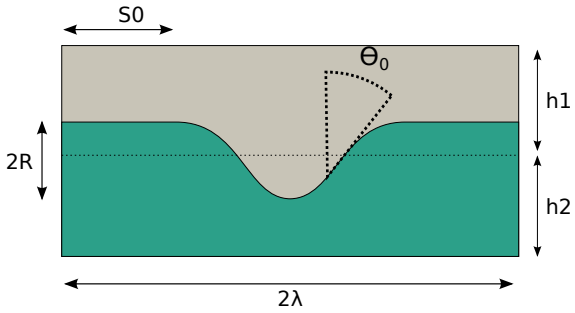


Figure 32: Roughness profile based on splines

is modeled by a rigid line. This will be used as reference solution for the contact since the rigid contact is easier to compute and gives more accurate results. Then, two other models with deformable contact are used, one with the same element density in each layer, another with a finer mesh inserted near the interface in the EMC layer. In each case, the unit cell has been loaded under shear loading ($\theta = 90°$) to create the most severe conditions for the contact. The response is x-periodic in the X and Y components of the reaction force with period $2\lambda$.

Table 6: Geometric, material and cohesive parameters for contact simulations

| Geometry | Cu | EMC | CZE |
|---|---|---|---|
| $\lambda = 8$ $\mu$m | height = 2R | height = 2R | $G_c = 0.010$ N/mm |
| R = 0.8 $\mu$m | E = 126.4 GPa | E = 19 GPa | $t_{max} = 10$ MPa |
| $S_0 = 3.52$ $\mu$m | $\nu = 0.33$ | $\nu = 0.35$ | |

The resulting traction-displacement curves are shown in figure 33. As expected, the rigid contact shows a higher value for the macroscopic reaction force. The curves for the deformable contact also have the same shape, which proves that the contact conditions are well respected. One can also notice that the model with local refinement at the interface gives a better definition of the contact. For the rigid contact and the deformable contact including a local refinement on the interface, we can observe from the reaction force - displacement curve that a very refined model is not required in order obtain an accurate solution.

Figure 34 shows that the continuity of the stress field at the interface is slightly altered by the presence of the inserts. This can be seen with the small oscillations on the curve 34c. Because these oscillations are not detectable in the macroscopic response, these oscillations can be neglected. Thus, all simulations involving contact between the two layers will be performed on a model with local refinement in the EMC layer from now on.

## *5.3 Results on a rough Cu-EMC interface*

The homogenization method, enhanced with the improvements for the contact definition, is now applied for an actual rough Cu-EMC interface. The objective of this section is to capture the different dissipative effects happening on a microscopic scale. In the following subsections, we will first focus on the effects of the roughness on the macroscopic cohesion by using elastic behavior on each layer. Then, plasticity will be added in the copper layer. Finally, we will have a look at the effects of the friction at the interface.

### 5.3.1 Elastic behavior

Other studies have already been performed to extract the adhesive properties of rough interface between two elastic materials having the same properties [28, 37]. In their approach, they compute macroscopic adhesive properties by investigating the effects of a crack propagating at the interface. The effects of several parameters is investigated, including the influence of the microscopic adhesive properties. The studies suggest that the effects of the roughness profile are only visible for a substantially brittle interface, i.e. having a small critical length value with respect to the roughness dimension and a high strength with

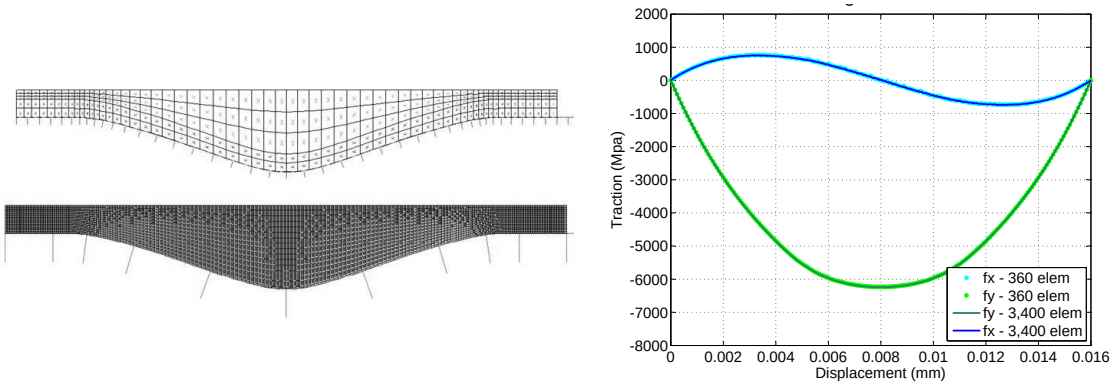


(a) Coarse (360 elements) and fine (3400 elements) meshing for rigid contact simulation

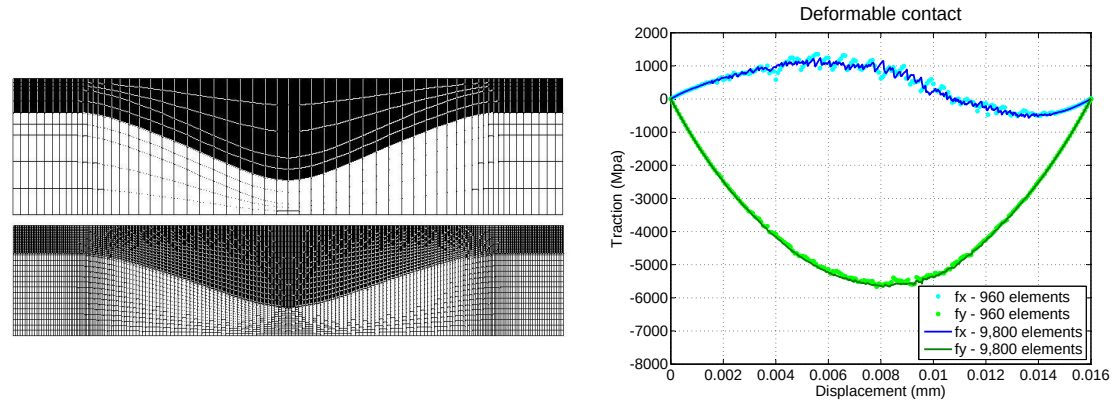


(b) Coarse (960 elements) and fine (9,800 elements) meshing for deformable contact simulation with regular mesh

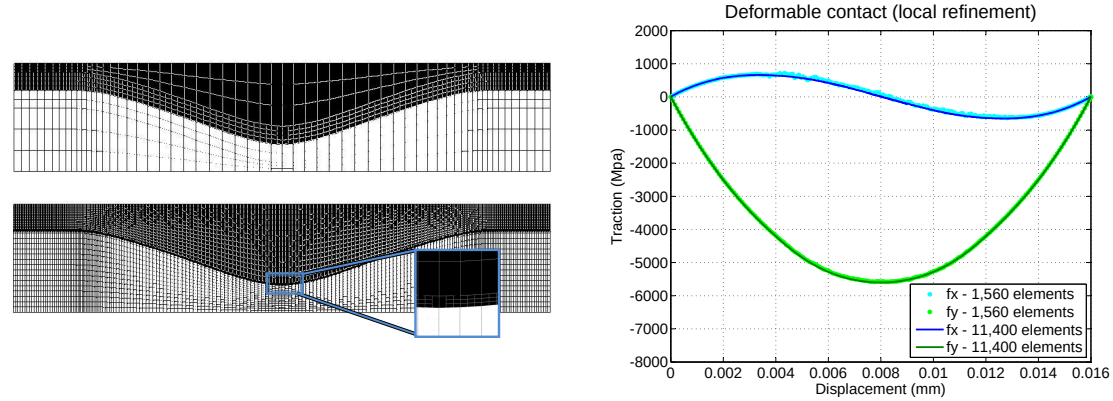


(c) Coarse (1,560 elements) and fine (11,400 elements) meshing for deformable contact simulation with locally refined mesh

Figure 33: Traction-displacement curves for a rough profile based on splines under shear loading.

respect to the layers stiffness. This can be explained using the notion of process zone. It corresponds to the area in which the CZEs are passing from the undamaged to the damaged

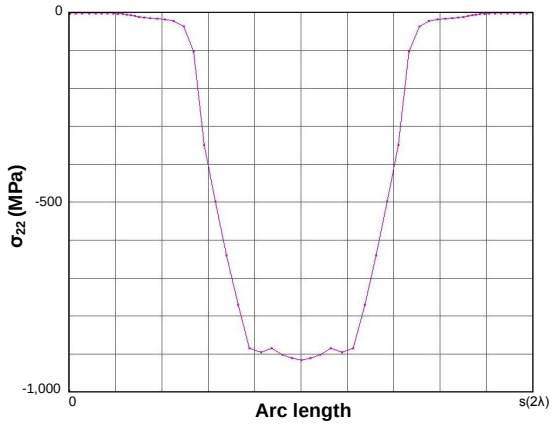


(a) Rigid contact

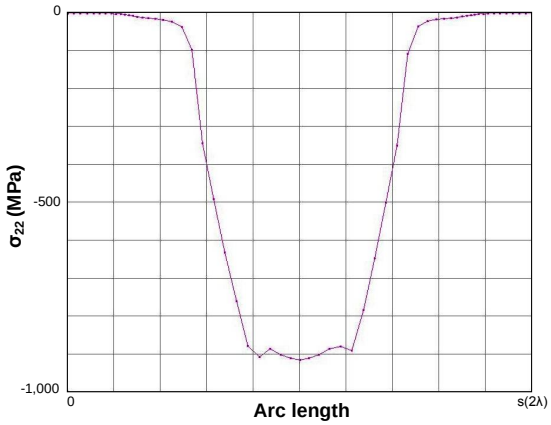


(b) Deformable contact with regular mesh

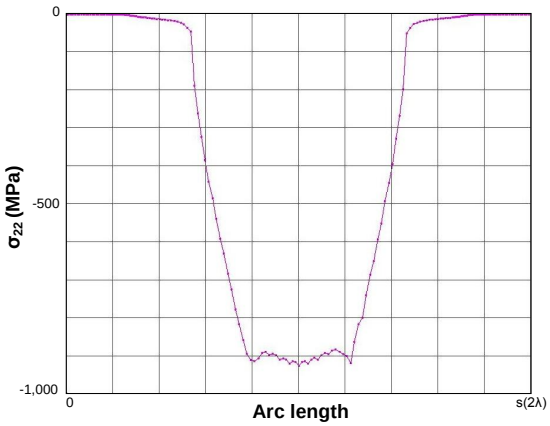


(c) Deformable contact with finer mesh inserted at the interface

Figure 34: y-component of the stress along the interface for a horizontal displacement equal to a half period of the roughness profile

state when the propagation of a crack is simulated. When the interface is brittle, the process zone becomes smaller. The tip of the crack is more localized which makes the delamination more sensible to the crack path, which is also the roughness profile. Indeed, the first results obtained in section 5.1.1 show that for a ductile interface, the results are only dependent on the change in area created by the roughness. The difficulty is that modeling brittle interfaces require a very robust solver to obtain converging solutions. For these reasons, larger values than what has been taken in section 5.1 are used for the next simulations. The strength value should however remain smaller than the loading limit of the EMC layer.

The materials and geometric properties for the unit cell are presented in table 7. The

simulations will be lead under different mode angles.

Table 7: Geometric and material parameters for elastic simulations

| Geometry | Cu | EMC |
|---|---|---|
| $\lambda = 8$ $\mu$m | height = 2R | height = 2R |
| R = 0.8 $\mu$m | E = 83.275 GPa | E = 19 GPa |
| $S_0 = 3.52$ $\mu$m | $\nu = 0.3$ | $\nu = 0.35$ |

The first simulations have been computed for different mode angle values below $\theta_c$ (see figure 32) from 0° to 70°. Another simulation has been added, labeled as "sliding" in table 8 in which the copper layer is constrained to slide on the interface, similar to the investigation on the triangular interface (see figure 24). Additional simulations have been done for mode angles of 75° and 80°. The microscopic interface toughness is $G_c^m = 0.02$ N/mm for all simulations. The microscopic interface strength $\tau_{max}^m$ has been chosen from 50 MPa to 150 MPa. The simulation would not be realistic if the the strength were higher, since we would be too close to the rupture point of the EMC.

Table 8: Effect of the microscopic strength on the homogenized values for $\theta \leqslant \theta_c$

| | $\tau_{max}^m = 50$ MPa | | | $\tau_{max}^m = 100$ MPa | | |
|---|---|---|---|---|---|---|
| $\theta$ | $G_c^M$ (N/m) | $\tau_{max}^M$ (MPa) | $\lambda_c^M$ (nm) | $G_c^M$ (N/m) | $\tau_{max}^M$ (MPa) | $\lambda_c^M$ (nm) |
| 0° | 20.57 | 51.45 | 147.1 | 20.58 | 103.04 | 80.9 |
| 20° | 20.58 | 51.49 | 154.5 | 20.63 | 103.14 | 80.9 |
| 40° | 20.60 | 51.54 | 154.5 | 20.67 | 102.77 | 88.3 |
| 60° | 20.60 | 51.54 | 154.5 | 20.69 | 102.66 | 95.6 |
| 70° | 20.60 | 51.55 | 161.9 | 20.65 | 102.57 | 99.3 |
| sliding | 21.70 | 54.28 | 160.2 | 21.38 | 103.29 | 103.3 |
| 75° | 21.10 | 51.70 | 161.9 | 21.10 | 103.30 | 95.6 |
| 80° | 22.40 | 51.50 | 161.9 | 21.40 | 103.20 | 103.0 |

| | $\tau_{max}^m = 150$ MPa | | |
|---|---|---|---|
| $\theta$ | $G_c^M$ (N/m) | $\tau_{max}^M$ (MPa) | $\lambda_c^M$ (nm) |
| 0° | 20.57 | 154.0 | 58.8 |
| 20° | 20.67 | 154.0 | 61.3 |
| 40° | 20.88 | 153.7 | 66.2 |
| 60° | 20.93 | 152.9 | 78.5 |
| 70° | 20.83 | 152.3 | 83.4 |
| sliding | 21.34 | 155.9 | 90.9 |
| 75° | 21.10 | 153.2 | 83.4 |
| 70° | 21.40 | 153.0 | 88.3 |

One can observe that the influence of the mode angle increases with the value of the

microscopic interface strength. The results show that the macroscopic toughness increases slightly either the mode angle of the microscopic strength rises. However, when the mode angle changes, only the value of the critical displacement is significantly modified. Figure 35 shows the effects on the macroscopic TSL.

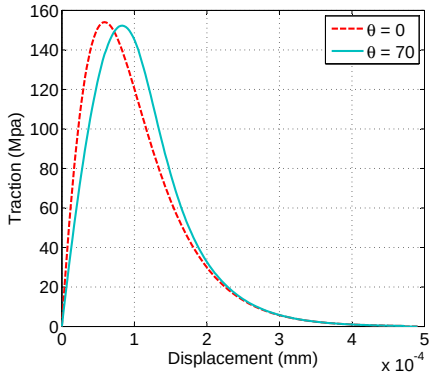


Figure 35: Increase of the macroscopic critical displacement with the mode angle. Here are presented the results for a microscopic interface strength of 150 MPa.

When the simulation have been performed for mode angles 75° and 80°, the method used was the same as the other mode angles. Here, the two layers are deforming because of the contact during the separation. It results in an elastic response to which is added the behavior of the interface, illustrated in figure 36.

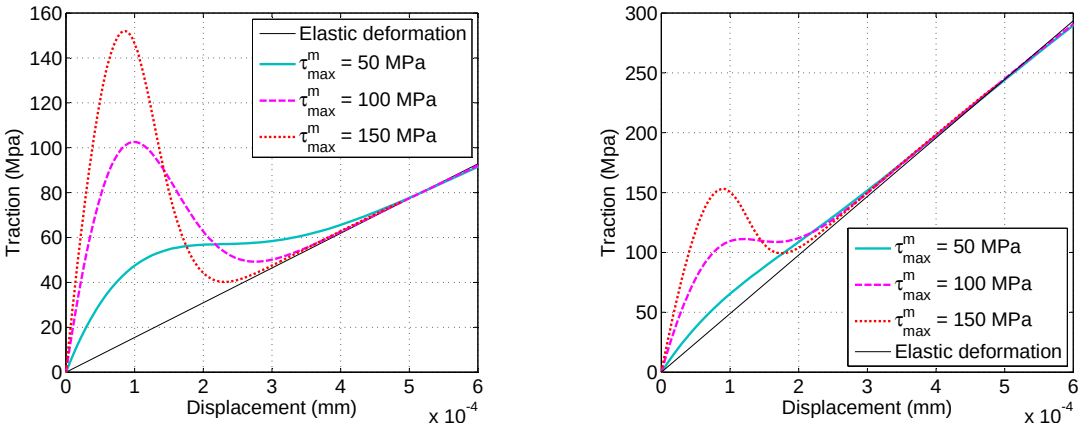


(a) $\theta$=75° (b) $\theta$=80°

Figure 36: Macroscopic TSL when the separation occurs for $\theta > \theta_c$

The difficulty has been to remove the contribution of the deformation of the bulk layers from the curve in order to define homogenized cohesive parameters for these simulations. To do so, we have performed a loading-unloading simulation on the RVE. The RVE has been loaded in displacement with a mode angle $\theta$, as usual, until the CZE at the interface can be considered as totally damaged. We consider the CZE totally damaged when the imposed displacement reaches ten times the critical length of the CZE. Then, the same displacement has been applied, but in the opposite direction to come back in the original configuration. Since the elastic contribution is the same for the loading or the unloading, the path defined by the traction displacement curve during the unloading is identified as the actual elastic contribution. In order to obtain the macroscopic TSL, the elastic contribution in the x and y components of the traction has been removed to come up with corrected curves, see figure 37. Taking the square mean of these two curves gives the expected result.

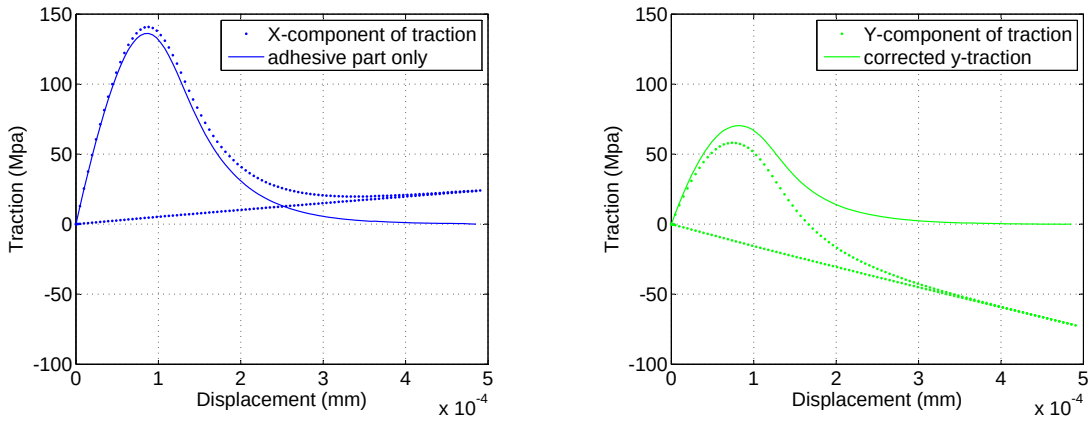


(a) X-component of the macroscopic traction

(b) Y-component of the macroscopic traction

Figure 37: Removal of the contribution of the elastic deformation of the two bulk layers on each component of the macroscopic traction. In this example, $\tau^m_{max} = 150$ MPa and $\theta$=75°.

### 5.3.2 Plasticity in the Cu layer

We are now using an elasto-plastic behavior for the copper layer [38]. The elastic properties remain the same as shown in table 7, but an additional evolution of the yield stress is

included (see figure 38), provided by [31]. These investigations are similar to the results of the previous section.

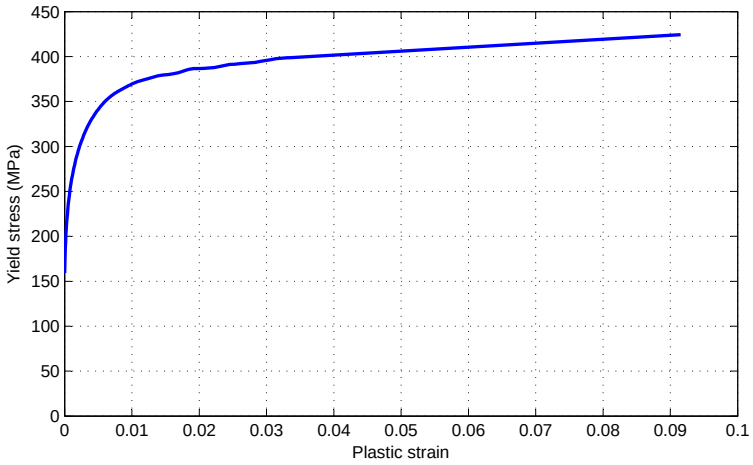


Figure 38: Plasticity law integrated in the Cu layer [31]

The results of the macroscopic cohesive parameters are presented in table 9 for the separations without a deformation of the layers due to the contact. In order to have visible effects of the plastic deformation of the metal, a high value has been chosen for the interface strength (150 MPa).

Table 9: Effect of the microscopic strength on the homogenized values for $\theta \leqslant \theta_c$, plasticity represented in the copper layer

| | $\tau_{max}^m = 150$ MPa | | |
|---|---|---|---|
| $\theta$ | $G_c^M$ (N/m) | $\tau_{max}^M$ (MPa) | $\lambda_c^M$ (nm) |
| 0° | 20.60 | 154.2 | 58.8 |
| 20° | 20.68 | 154.0 | 61.3 |
| 40° | 20.88 | 153.7 | 66.2 |
| 60° | 21.05 | 153.1 | 78.5 |
| 70° | 21.08 | 152.6 | 83.4 |
| sliding | 21.34 | 155.9 | 90.9 |

Table 9 allows us to say that for a separation with a mode angle below $\theta_c$, the toughness is increased due to the dissipation of energy when the copper deforms plastically. However, the improvements are not tremendous in this case since the copper do not deform much in comparison to the EMC layer.

When the separation occurs with deformation of the bulk layer, we have tried the same

method as previously to extract the macroscopic TSL. Figure 39 shows the curves of the X and Y components of the macroscopic traction when the mode angle is 75 and 80°. The curves have been compared with the results for an elastic behavior only in the copper. During the separation, the copper undergoes permanent plastic deformations. Because of that, when the EMC layer is constrained to come back at its originate position after the CZE have been totally damaged, the roughness profile is modified and additional deformations are also occurring. This effect is more pronounced for $\theta = 80°$. Because of that, the unloading path cannot be used here to extract the macroscopic TSL.

### 5.3.3 Friction at the interface

In this section, we will investigate the effects of the friction, modeled as was described in section 2.3.2, with a friction coefficient $\mu = 0.1$. The simulations are performed for the "sliding" configuration and for load angles of 75° and 80°. To have a better representation of the effects of the friction stresses at the interface, the adhesion microscopic interface strength $\tau_m$ has been set to 50 MPa to reduce the influence of the microscopic adhesion forces in the macroscopic response.

Table 10: Influence of the friction on the homogenized cohesive values from adapted TSL for sliding configuration

| | Elastic copper | | | Elasto-plastic copper | | |
|---|---|---|---|---|---|---|
| $\theta$ | $G_c^M$ (N/m) | $\tau_{max}^M$ (MPa) | $\lambda_c^M$ (nm) | $G_c^M$ (N/m) | $\tau_{max}^M$ (MPa) | $\lambda_c^M$ (nm) |
| sliding | 22.43 | 55.96 | 160.2 | 22.43 | 55.96 | 160.2 |

For the "sliding" configuration, the results clearly show that the friction improves the macroscopic adhesion of the interface, as confirmed by figure 40.

When the simulations are performed for a mode angle beyond $\theta_c$, we also observe that energy dissipation occurs when the EMC layer is constrained to come back to its origin. When we look at each component of the macroscopic traction (see figure 41), we have a better understanding of what is happening. The friction adds additional stress compared to the relative displacement of the interface. For this reason, the x-component, compared to the separation, is increased by the friction, and the y-component, favoring the separation, in reduced.

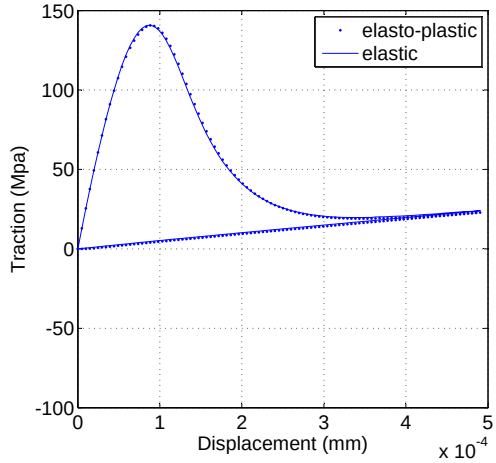


(a) X-component of the macroscopic traction for $\theta$=75°

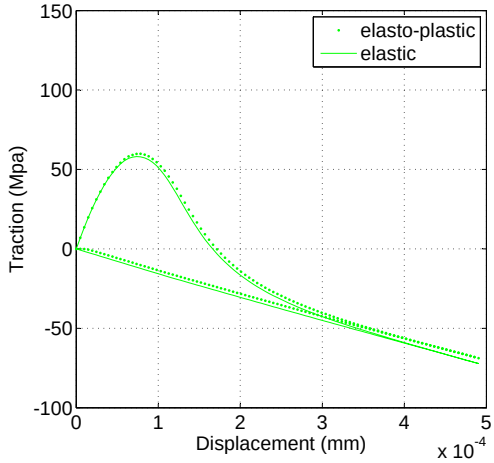


(b) Y-component of the macroscopic traction for $\theta$=75°

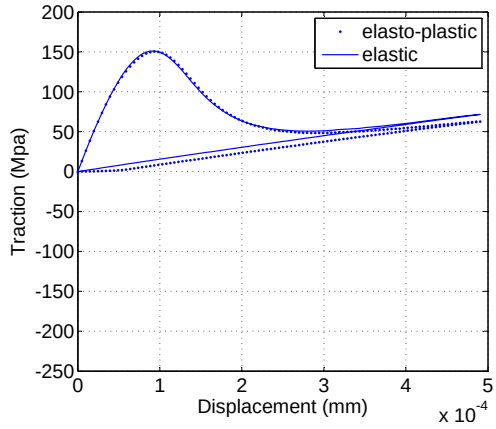


(c) X-component of the macroscopic traction for $\theta$=80°

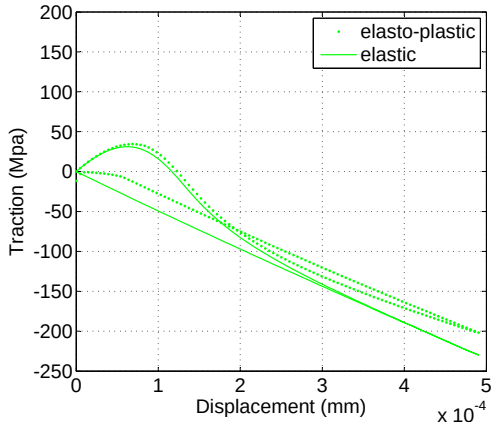


(d) Y-component of the macroscopic traction for $\theta$=80°

Figure 39: Influence of plasticity on the macroscopic TSL when the separation occurs for $\theta > \theta_c$

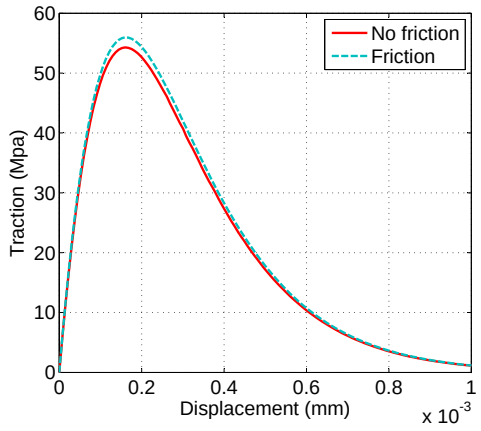


Figure 40: Influence of the friction at the interface on the macroscopic TSL in sliding configuration

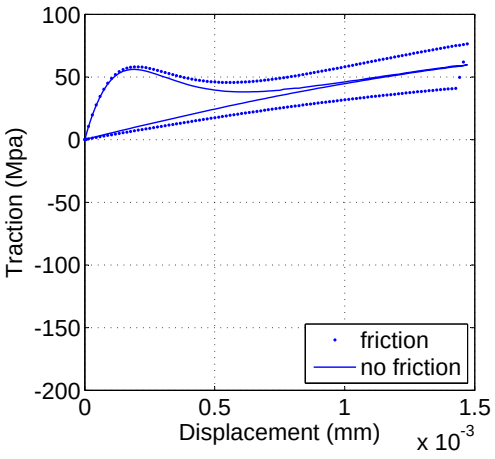


(a) Elastic behavior for the copper layer and $\theta$=75°

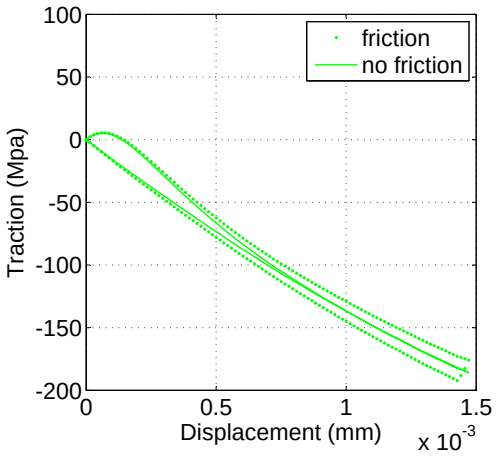


(b) Elastic behavior for the copper layer and $\theta$=75°

Figure 41: X and Y components of the macroscopic reaction for elastic and elasto-plasctic copper.

# CHAPTER VI

# CONCLUSIONS AND FUTURE WORK

In this study, a homogenization method was developed to extract the cohesive properties of a rough interface between two materials using a finite element model that includes several dissipative effects, such as the cohesion at the interface, the plasticity inside the bulk material and the friction at the interface. The traction-displacement curve of the interface was drawn and the cohesive parameters, such as the interface toughness and strength, were extracted. Different mode angles were investigated, and two sets of boundary conditions were proposed for the normal loading. These results were compared to the solutions from the DCB and the 3ENF tests, two benchmark tests widely used for the experimental determination of the interface toughness, respectively under modes I and II.

This method aims at being applied to a rough metal-polymer interface. Several simplified simulations have been performed, however, it was not possible to model the softening of the bulk material and include processes similar to crack kinking because of numerical issues. In the simulations, the only implemented damage process was the cohesion at the interface. Other dissipative processes, plasticity and friction, were investigated. The Representative Volume Element was loaded under several loading modes. A "critical mode angle" was defined as the limit between separation with or without contact occurring between the two bulk layers. When the separation is occurring for a mode angle above this critical mode angle, the macroscopic cohesive properties were not directly accessible because of the additional reaction force generated from the contact forces preventing the penetration of the mesh of one the layers into the other one.

The first investigations revealed that for a soft interface, the enhanced cohesive properties were only dependent on the augmentation of the contact area involved by the roughness profile. With the increase of the interface strength of the CZEs, the study revealed the mode angle dependency of the macroscopic cohesive properties. In particular, the macroscopic

critical displacement is sensitive to the other parameters. The study of the dissipative mechanisms has shown, for this model, that the macroscopic toughness was actually increasing when the friction or the plasticity in the copper was used. Under the assumption of a fragile layer of EMC, the friction is still more likely to affect the macroscopic adhesive properties since it would be difficult to deform plastically the copper layer without damaging the EMC layer first.

This study showed that the method proposed to extract the macroscopic Traction-Separation Law of a rough interface was able to capture the effects of the dissipative effects of the friction and the plasticity. It did, however, show some difficulties to extract the macroscopic cohesive properties when contact is occurring between the layers when dissipative mechanisms were modeled. One solution for this problem could be, for example, the definition of others unloading condition. Otherwise, one could try an alternative to the choice of the periodic boundary conditions for the RVE by exploring the minimal kinematic boundary conditions [22, 12].

# REFERENCES


[1] Alfaro, M. C., Suiker, A., Verhoosel, C., and de Borst, R., "Numerical homogenization of cracking processes in thin fibre-epoxy layers," *European Journal of Mechanics - A/Solids*, vol. 29, no. 2, pp. 119 – 131, 2010.

[2] Andersson, T. and Stigh, U., "The stress-elongation relation for an adhesive layer loaded in peel using equilibrium of energetic forces," *International Journal of Solids and Structures*, vol. 41, no. 2, pp. 413–434, 2004.

[3] Chandra, N., Li, H., Shet, C., and Ghonem, H., "Some issues in the application of cohesive zone models for metal-ceramic interfaces," *International Journal of Solids and Structures*, vol. 39, no. 10, pp. 2827–2855, 2002.

[4] Davies, P., Blackman, B., and Brunner, A., "Standard test methods for delamination resistance of composite materials: current status," *Applied Composite Materials*, vol. 5, no. 6, pp. 345–364, 1998.

[5] Engerand, J., "Mécanique de la rupture," *Techniques de l'ingénieur. Génie mécanique*, no. B5060, pp. 1–12, 1990.

[6] Eshelby, J. D., "The elastic energy-momentum tensor," *Journal of Elasticity*, vol. 5, pp. 321–335, 1975.

[7] Goyal, V., *Analytical modeling of the mechanics of nucleation and growth of cracks.* PhD thesis, Virginia Polytechnic Institute and State University, 2002.

[8] Griffith, A., "The phenomena of rupture and flow in solids," *Philosophical Transactions of the Royal Society of London.*, vol. 221, pp. 163–198, 1920.

[9] Hill, R., "The essential structure of constitutive laws for metal composites and polycrystals," *Journal of the Mechanics and Physics of Solids*, vol. 15, no. 2, pp. 79–95, 1967.

[10] Hirschberger, C., Ricker, S., Steinmann, P., and Sukumar, N., "Computational multiscale modelling of heterogeneous material layers," *Engineering Fracture Mechanics*, vol. 76, no. 6, pp. 793–812, 2009.

[11] Hirschberger, C., Sukumar, N., and Steinmann, P., "Computational homogenization of material layers with micromorphic mesostructure," *Philosophical Magazine*, vol. 88, no. 30, pp. 3603–3631, 2008.

[12] Inglis, H., Geubelle, P., and Matouš, K., "Boundary condition effects on multiscale analysis of damage localization," *Philosophical Magazine*, vol. 88, no. 16, pp. 2373–2397, 2008.

[13] Irwin, G., "Relation of stresses near a crack to the crack extension force," in *Int. Congress on Applied Mech. Bruxelles*, p. 245, 1956.

[14] Irwin, G., "Analysis of stresses and strains near the end of a crack traversing a plate.," *Journal of applied mechanics*, p. 361, 1957.

[15] Jianmin, Q. and Cherkaoui, M., *Fundamentals of micromechanics of solids*. New York: Wiley, 2006.

[16] Kolluri, M., Hoefnagels, J., van Dommelen, J., and Geers, M., "Modeling and characterization of irreversible mixed mode interface delamination using a cohesive zone with combined damage and plasticity," *Engineering Fracture Mechanics*, 2010.

[17] Koninklijke Philips Electronics, N., "Nano Interface." http://www.nanointerface.eu/, 2004-2011.

[18] Krueger, R., "Virtual crack closure technique: History, approach, and applications," *Applied Mechanics Reviews*, vol. 57, p. 109, 2004.

[19] Li, S., "Boundary conditions for unit cells from periodic microstructures and their implications," *Composites Science and Technology*, vol. 68, no. 9, pp. 1962–1974, 2008.

[20] Malvern, L., "Introduction to the Mechanics of a Continuous Medium," *Englewood Cliffs*, 1969.

[21] Matouš, K., Kulkarni, M., and Geubelle, P., "Multiscale cohesive failure modeling of heterogeneous adhesives," *Journal of the Mechanics and Physics of Solids*, vol. 56, no. 4, pp. 1511–1533, 2008.

[22] Mesarovic, S. and Padbidri, J., "Minimal kinematic boundary conditions for simulations of disordered microstructures," *Philosophical Magazine*, vol. 85, no. 1, pp. 65–78, 2005.

[23] Msc Software, *Marc 2008r1 - Volume A: Theory and User Information*, 2008.

[24] Noijen, S., van der Sluis, O., Timmermans, P., and Zhang, G., "Numerical prediction of failure paths at a roughened metal/polymer interface," *Microelectronics Reliability*, vol. 49, no. 9-11, pp. 1315–1318, 2009.

[25] Olsson, P. and Stigh, U., "On the determination of the constitutive properties of thin interphase layers - an exact inverse solution," *International journal of fracture*, vol. 41, no. 4, pp. 71–76, 1989.

[26] Ortiz, M. and Pandolfi, A., "Finite-deformation irreversible cohesive elements for three-dimensional crack-propagation analysis," *International Journal for Numerical Methods in Engineering*, vol. 44, no. 9, pp. 1267–1282, 1999.

[27] Qu, J., "Mechanics of interfaces in microelectronic packaging," tech. rep., G.W. Woodruff School of Mechanical Engineering,Georgia Institute of Technology, 2009.

[28] Reedy, E., "Effect of patterned nanoscale interfacial roughness on interfacial toughness: A finite element analysis," *Journal of Materials Research*, vol. 23, no. 11, pp. 3056–3065, 2008.

[29] Salomonsson, K., "Mixed mode modeling of a thin adhesive layer using a mesomechanical model," *Mechanics of Materials*, vol. 40, no. 8, pp. 665–672, 2008.

[30] Salomonsson, K. and Andersson, T., "Modeling and parameter calibration of an adhesive layer at the meso level," *Mechanics of Materials*, vol. 40, no. 1-2, pp. 48–65, 2008.

[31] van der Sluis, O., Hsu, Y., Timmermans, P., Gonzalez, M., and Hoefnagels, J., "Stretching-induced interconnect delamination in stretchable electronic circuits," *Journal of Physics D: Applied Physics*, vol. 44, p. 034008, 2011.

[32] Van Gils, M., van Der Sluis, O., Zhang, G., Janssen, J., and Voncken, R., "Analysis of Cu/low-k bond pad delamination by using a novel failure index," *Microelectronics Reliability*, vol. 47, no. 2-3, pp. 179–186, 2007.

[33] Van Hal, B., Peerlings, R., Geers, M., and van Der Sluis, O., "Cohesive zone modeling for structural integrity analysis of IC interconnects," *Microelectronics Reliability*, vol. 47, no. 8, pp. 1251–1261, 2007.

[34] Verhoosel, C., Remmers, J., Gutiérrez, M., and de Borst, R., "Computational homogenization for adhesive and cohesive failure in quasi-brittle solids," *International Journal for Numerical Methods in Engineering*, vol. 83, no. 8–9, pp. 1155–1179, 2010.

[35] Yao, Q. and Qu, J., "Interfacial versus cohesive failure on polymer-metal interfaces in electronic packagingeffects of interface roughness," *Journal of Electronic Packaging*, vol. 124, p. 127, 2002.

[36] Yoshihara, H., "Mode I and mode II initiation fracture toughness and resistance curve of medium density fiberboard measured by double cantilever beam and three-point bend end-notched flexure tests," *Engineering Fracture Mechanics*, 2010.

[37] Zavattieri, P., Hector, L., and Bower, A., "Determination of the effective mode-I toughness of a sinusoidal interface between two elastic solids," *International Journal of Fracture*, vol. 145, no. 3, pp. 167–180, 2007.

[38] Zavattieri, P., Hector Jr, L., and Bower, A., "Cohesive zone simulations of crack growth along a rough interface between two elastic-plastic solids," *Engineering Fracture Mechanics*, vol. 75, no. 15, pp. 4309–4332, 2008.